

Sky localization and polarization mode reconstruction of gravitational waves from GW170104 and GW150914

Oswaldo M. Moreschi^{1,2}

¹Facultad de Matemática, Astronomía, Física y Computación(FaMAF), Universidad Nacional de Córdoba, Ciudad Universitaria, Córdoba, (5000), Argentina.

²Instituto de Física Enrique Gaviola(IFEG), CONICET, Ciudad Universitaria, Córdoba, (5000), Argentina.

Contributing authors: o.moreschi@unc.edu.ar;

Abstract

The detections(Abbott et al, 2023, 2021) and analysis of gravitational waves(GWs) have introduced us in a new era of our understanding of the cosmos, providing new insights into astrophysical systems involving massive objects as black holes and neutron stars. Normally the precise sky localization of a GW source needs data from three or more observatories(Abbott et al, 2016c, 2017c). However, the results presented in this article demonstrate that it is in fact possible to obtain the position of a GW source in a small region of the celestial sphere using data from just two GW observatories, in this case LIGO Hanford and LIGO Livingston. Furthermore, we are also able to reconstruct the gravitational-wave polarization(Poisson and Will, 2014) modes(PMs) for the GW170104(Abbott et al, 2017b) and GW150914(Abbott et al, 2016a) events, with data from only these two detectors. The procedure only uses the spin 2 properties of the GW, so that it does not rely on specific assumptions on the nature of the source. Our findings are possible through careful data filtering methods(Moreschi, 2019), the use of refined signal processing algorithms(Moreschi, 2024), and the application of dedicated denoising(Mallat, 2009) techniques. This progress in the GW studies represents the first instance of a direct measurement of PMs using such a limited observational data. We provide detailed validation through the reconstruction of PMs for different polarization angles, and calculations of residuals for the GW170104 event. We also test the procedure with synthetic data with ten different source locations and polarization angles.

Keywords: Gravitational waves, Gravitational wave astronomy, Astronomy data analysis

2025-07-21 00:49:34Z

Contents

1	Introduction	2	6	Injected signals from synthetic spin-2 polarization modes	8
			6.1	Injected signals and denoised reconstruction	8
			6.2	Localization	12
			6.3	Reconstruction of the spin-2 polarization modes	15
2	Decomposition of a gravitational wave in terms of polarization modes	3	7	Localization of GW170104	16
3	Estimates of the signal by wavelet denoising of the strain	4	8	Reconstruction of the spin-2 polarization modes of GW170104	17
4	Study of the nature of the signals in the time-frequency domain	5	9	Complete reconstruction of the signal in terms of the spin-2 polarization modes for GW170104	18
5	Using a universal fitting chirp form for gravitational-wave polarization modes	6	10	Nominal time shift for GW150914	19

11 Study of GW150914 in the time-frequency domain	20
12 Localization of GW150914	21
13 Reconstruction of the spin-2 polarization modes of GW150914	21
14 Final comments	22
A Basic theoretical framework	24
B Basis and coordinate systems	26
C Basis for the calculation of the detector pattern functions	26
D Reference frames for the propagation of the gravitational wave	26
E Detector pattern functions for GW	27
F Fitting a universal chirp form	27
G Localization by fitting a universal chirp form	27
H Characteristics of the strain	28
I Determination of the appropriate time delay for the GW170104 event	28
J Other studies of GW170104	29
K Spin-2 polarization modes of GW170104 for different polarization angles	29
L Simulation using an injected simple signal	30

1 Introduction

The localization of transient GW sources on the celestial sphere involves several significant challenges, coming from both the nature of the signals and the characteristics of current observational infrastructure (Abbott et al, 2020; Singer and Price, 2016; Veitch et al, 2015). The sensitivity of GW detectors is affected by various sources of noise, including seismic activity, thermal fluctuations, and instrumental noise. These noises can hide the signals and complicate the process of determining the source location. For this reason, in our method, it is essential to handle the strains with appropriate pre-processing filtering techniques (Moreschi, 2019). Instead, for the detection problem, the Ligo-Virgo-Kagra (LVK) teams have elaborated a series of methods including matched filtering techniques (Allen et al, 2012) and unmodeled methods (Klimenko et al, 2011, 2016) that are used for LVK detection and localization without employing the just mentioned pre-processing filtering techniques. The accuracy of localizing a GW source improves with the

number of detectors and their geographical spread. Currently, the primary detectors are the two LIGO, Hanford and Livingston, the Virgo and the KAGRA observatories. Recording signals on three or more observatories helps considerably in determining the source location, since one can recur to the intersection of allowed sky regions, by using the time delay of arrival among the observatories; diminishing in this way the probable localization area on the celestial sphere. Other issues that are involved in the precision to locate the sources are the relative signal amplitude calibration and the phase consistency between detectors (Abbott et al, 2020). The amount of information that one can obtain from a GW observation increases considerably when it can be related to multimessenger observations. For this reason some efforts (Chatterjee et al, 2023; Kolmus et al, 2022; You et al, 2021; Hu et al, 2021; Tsutsui et al, 2021; Singer and Price, 2016) are directed to optimize the time required to indicate the localization of GW sources. In general, all these techniques involve the Bayesian statistical framework that require the choice of priors for the nature of the source; nevertheless, the cWB pipeline (Klimenko et al, 2011, 2016) uses a model-independent approach which is able to provide sky localization based on coherent signal power. The approach described below, does not use specific templates neither we use information on individual masses, but rather we use a universal chirp form for the inspiral phase, and so in this sense it is model independent.

The expression of a GW in terms of its polarization modes (Poisson and Will, 2014) is one of the most fundamental aspects involved in the detection process and its analysis. Consequently it is the subject of constant discussion in the literature. In particular in reference Eardley et al (1973b) and Eardley et al (1973a) they treated PMs for the specific case of plane waves. Some of the efforts in the literature have concentrated on the separability of the polarization modes with a limited number of gravitational-wave detectors (Takeda et al, 2018). In Abbott et al (2018) they have carried out a search for a stochastic background of generically polarized gravitational waves; where they found no evidence for a background of any polarization, placing bounds on the contributions of vector and scalar polarizations to the stochastic background. In Gürsel and Tinto (1989) the authors presented a theoretical method for determining the source direction in the sky and the two polarization modes of a GW that require to use the data from three detectors. This approach has been extended in several directions (Chatterji et al, 2006). We improve on these types of approaches, since we here introduce a procedure for the sky localization with two detectors and the gravitational-wave polarization modes reconstruction (L2D+PMR) of the signal. We thus provide first explicit measurements of the spin-2 polarization modes of a gravitational wave.

This article is dedicated to the presentation of the procedure L2D+PMR, and it is applied to the GW170104 and

GW150914 events as a case studies. We will devote future work to extract physical information from these events.

The GW170104 event has strong enough signals and low enough noise which we can use to develop and apply our procedure, and allows us to extract the spin-2 polarization modes of the detected GW. Actually the reconstruction of the PMs can only be achieved if one can also localize the direction in the sky of the source of the GW; it is for this reason that both problems must be solved synchronously. We do not mean here that one should carryout the localization and the reconstruction of PMs as a joint probability distribution; instead we do the localization first by using partial properties of the polarization modes and the delay time information. In addition, in order to show how robust and effective is our method, we also apply it to reconstruct the signal, the polarization modes and to find the localization of the source for a simple injected signal, starting from the corresponding synthetic spin-2 polarization modes with 10 chosen positions for the hypothetic source and with different polarization frames for each of them.

We also apply the L2D+PMR procedure to the first GW detection, GW150914. This event was initially studied during the early stages of our work using a different measure, which presented several difficulties. To overcome these, we extended the analysis to later events, such as GW170104 and others involving three detectors (Moreschi, 2025). This expansion helped us to evolve and validate the method. The developed version now produces significant results for GW150914, which are presented below. Due to space constraints, we do not include a comprehensive analysis of GW150914 in this work; a detailed examination of this event's physical characteristics will be addressed in future research.

We here advance a sketch of the L2D+PMR procedure that is going to be presented and applied along the article.

The L2D+PMR procedure:

- **Selection of Strains:** Choose the strains with the least amount of prior filtering for the event under study.
- **Pre-Processing Filtering:** Apply pre-processing filtering techniques (Moreschi, 2019).
- **Window Selection:** Select a window length wl for the detailed study of the signals.
- **Time delay:** Determine the appropriate working time delay between the observatories from a careful study of the signal. (See section I.)
- **Chirp times:** Found the characteristic chirp times from a study of the signals in the time-frequency domain.
- **Bandpass filter:** Apply an appropriate bandpass filter to the strains data following time-frequency domain analysis.
- **Denoising:** Denoise each strain using wavelets techniques (Section 3).
- **Source Localization:** Determine the localization of the source using data from two observatories, as detailed in this article. If more than two observatories provide data

for the event, iterate this procedure and calculate the final localization.

- **Polarization Mode Reconstruction:** Reconstruct the polarization modes of the gravitational wave using the algebra we present.

For the organization of this article, we present our results and essential structure in the main text, and relegate to the appendices a series of detailed explanations of some points mentioned in the text. In section 2 we present the basic algebra used in the decomposition of the signals in terms of polarization modes. Section 3 is devoted to the presentation of the denoising of the signals. In section 4 we show the study of the GW in the time-frequency domain. We describe how to fit a universal chirp form to a signal in section 5. To validate our methods, we study in section 6 the localization of ten sources and the corresponding reconstruction of the spin-2 polarization modes. The result of the sky localization of the source of the GW for event GW170104 is presented in 7. In section 8 we present explicitly, as time series, the polarization modes of the GW of the GW170104 event. We show that these spin-2 polarization modes account for the complete reconstruction of the gravitational wave in section 9; that is we measure no contribution coming from polarization modes with spin 1 or 0 to GW170104. The study of the nominal time shift of strain H with respect to L for GW150914 is presented in section 10. Section 11 is devoted to the analysis of GW150914 in the time-frequency domain. In section 12 we present the result of the localization of GW150914. The reconstruction of the + and \times polarization modes of GW150914 is presented in section 13. In section 14 we present some final comments. And, as said above, in several appendices we present some details of topics discussed in the main part.

2 Decomposition of a gravitational wave in terms of polarization modes

Having a detection of a GW in two observatories, in our case H (Hanford) and L (Livingston), one has in each of them the recorded strain

$$\begin{aligned} v_X(t + \tau_X) &= n_X(t + \tau_X) + s_X(t + \tau_X) \\ &= n_X(t + \tau_X) + F_{+X}(\theta_X, \phi_X, \psi_X, t) s_+(t) \\ &\quad + F_{\times X}(\theta_X, \phi_X, \psi_X, t) s_\times(t), \end{aligned} \quad (1)$$

where X stands for H or L , τ_X is the time delay of detector X with respect to the chosen reference observatory, (θ_X, ϕ_X) are the angular coordinates with respect to detector X of the direction of the source, ψ_X is the angle of the GW frame and t is the time. The strain is denoted by v , we use n to refer to the noise, s for the signal, which is decomposed in the PMs s_+ and s_\times ; while F_+ and F_\times are the detector pattern functions discussed in appendix E.

Being a little bit more generic, let us denote with D and E two detectors where one has recorded the signals of a GW. Let (δ, α) be an arbitrary direction in the celestial sphere, and (δ_0, α_0) the location of the source. Then, we define

$$\begin{aligned} v_{+DE}(\delta, \alpha, t) &= v_D(t + \tau_D)F_{\times E}(\delta, \alpha, t) \\ &\quad - v_E(t + \tau_E)F_{\times D}(\delta, \alpha, t) \\ &= n_{\times DE} + (F_{\times E}F_{+D0} - F_{\times D}F_{+E0})s_+(t) \\ &\quad + (F_{\times E}F_{\times D0} - F_{\times D}F_{\times E0})s_{\times}(t), \end{aligned} \quad (2)$$

where we are using the notation $F_{\times D} \equiv F_{\times D}(\delta, \alpha, t) = F_{\times D}(\theta_D(\delta, \alpha), \phi_D(\delta, \alpha), \psi_D(\delta, \alpha), t)$ and $F_{\times D0} \equiv F_{\times D}(\delta_0, \alpha_0, t)$; where we are considering $(\delta, \alpha) \neq (\delta_0, \alpha_0)$. Then, when evaluated at the source position (δ_0, α_0) one would obtain a strain of the form:

$$\begin{aligned} v_{+DE}(\delta_0, \alpha_0, t) &= F_{\times E}(\delta_0, \alpha_0, t) \\ &\quad (n_D(t + \tau_D) + F_{+D}(\delta_0, \alpha_0, t)s_+(t) \\ &\quad - F_{\times D}(\delta_0, \alpha_0, t) \\ &\quad (n_E(t + \tau_E) + F_{+E}(\delta_0, \alpha_0, t)s_+(t))) \\ &= n_{\times DE}(t) + (F_{\times E0}F_{+D0} - F_{\times D0}F_{+E0})s_+(t) \\ &= n_{\times DE}(t) + f_{+0}s_+(t), \end{aligned} \quad (3)$$

without the cross contribution, and where $f_{+0} = F_{\times E0}F_{+D0} - F_{\times D0}F_{+E0}$ and

$$\begin{aligned} n_{\times DE}(\delta, \alpha, t) &= F_{\times E}(\delta, \alpha, t) \times n_D(t + \tau_D) \\ &\quad - F_{\times D}(\delta, \alpha, t) \times n_E(t + \tau_E). \end{aligned} \quad (4)$$

In an analogous way we can select the \times mode. We define

$$\begin{aligned} v_{\times DE}(\delta, \alpha, t) &= v_D(t + \tau_D)F_{+E}(\delta, \alpha, t) \\ &\quad - v_E(t + \tau_E)F_{+D}(\delta, \alpha, t) \\ &= n_{+DE} + (F_{+E}F_{+D0} - F_{+D}F_{+E0})s_+(t) \\ &\quad + (F_{+E}F_{\times D0} - F_{+D}F_{\times E0})s_{\times}(t), \end{aligned} \quad (5)$$

where we have used the notation $F_{+D}(\delta, \alpha, t) = F_{+D}(\theta_D(\delta, \alpha), \phi_D(\delta, \alpha), \psi_D(\delta, \alpha), t)$. Then, when evaluated at the source position (δ_0, α_0) one would obtain a strain of the form:

$$\begin{aligned} v_{\times DE}(\delta_0, \alpha_0, t) &= n_{+DE}(t) + (F_{+E0}F_{\times D0} - F_{+D0}F_{\times E0})s_{\times}(t) \\ &= n_{+DE}(t) + f_{\times 0}s_{\times}(t) = n_{DE}(t) - f_{+0}s_{\times}(t), \end{aligned} \quad (6)$$

without the plus contribution, and where

$$\begin{aligned} n_{+DE}(\delta, \alpha, t) &= F_{+E}(\delta, \alpha, t) \times n_D(t + \tau_D) \\ &\quad - F_{+D}(\delta, \alpha, t) \times n_E(t + \tau_E), \end{aligned} \quad (7)$$

and where we have noted that $f_{\times 0} = -f_{+0}$. It should be noted that all manipulations to obtain the polarization modes come from the relations expressed in (1); however, the approach we use through our definitions (2) and (5) is very different from the inverse problem approach described in [Gürsel and Tinto \(1989\)](#) where they assume data is recorded in three observatories.

Associated to a time delay between the observatories, which is described in appendix I; there is a ‘delay ring’ in the sky showing the theoretical possible locations of the source. The determination of the delay ring involves an intrinsic error which comes from the error in the time delay value. In appendix I we discuss to possible origins for errors. This in

turn generates an uncertainty on the determination of the angle for the ring. With this we can construct a Gaussian distribution around the delay ring with the intention of giving a representation of the error in the ring determination, as shown in Fig. 1.

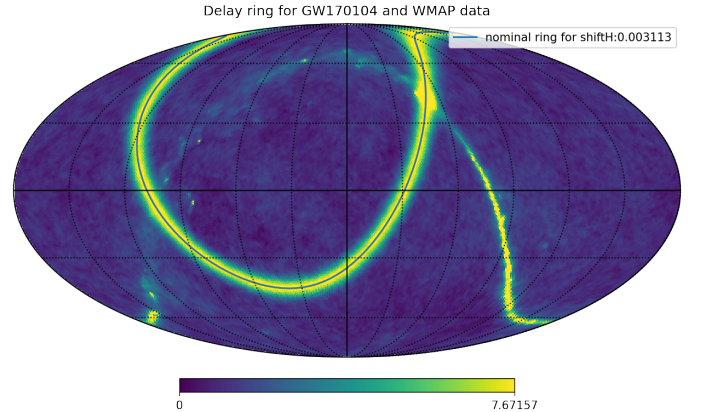


Fig. 1 Estimate of the probability distribution for the localization of the gravitational-wave source, considering the information encoded in the measurement of the delay ring. The background with the WMAP data is included to show the nature of the Mollweide projection being used; in equatorial coordinates with origin at center and East to the left.

The Gaussian region of the delay ring represents an estimate of the probability distribution for the sky localization of the source of the GW based on time delay considerations. When an independent localization technique, such as the L2D+PMR procedure, is applied, one would expect to find the estimated source position near or within this Gaussian region. As we will demonstrate in sections 7 and 12, this is precisely what occurs when we apply the L2D+PMR method to two real events. In Fig. 1 we also include the image of our Galaxy, through a WMAP graph, in order to clarify the nature of the celestial coordinates and the location of its origin. We discuss further the time delay ring in appendix I.

3 Estimates of the signal by wavelet denoising of the strain

Previously we have been working with the observed strains directly. This has the advantage of dealing with filtered observed data, but it has the disadvantage that it is difficult to estimate the strength of the signals due to the ambient noise. For this reason we also consider the estimate of the signal at each detector, by applying wavelet denoising techniques. In this way we arrive now at the estimates:

$$\begin{aligned} w_X(t + \tau_X) &= e_X(t + \tau_X) + s_X(t + \tau_X) \\ &= e_X(t + \tau_X) + F_{+X0}(\theta_X, \phi_X, \psi_X, t)s_+(t) \\ &\quad + F_{\times X0}(\theta_X, \phi_X, \psi_X, t)s_{\times}(t), \end{aligned} \quad (8)$$

where w_X are the estimates, and now e_X stands for the error intrinsic to the estimates. Contrary to the previous situation, discussed in the previous section, now we assume that

the magnitude of the errors are much smaller than the magnitude of the signals. That is, we can neglect them in the localization process; although we estimate them from the calculation of the sample standard deviation with respect to v_X on a chosen window. We chose this approach because it provides time dependent values, which adapt to the characteristics of the signal dynamically. We will also assume that the scalar product of the error with the signals are negligible. These assumptions are supported from the results of Donoho and Johnstone (Donoho and Johnstone, 1994; Mallat, 2009) on thresholding estimators; and also from the numerical estimation of the errors.

The technique for inferring the signals by applying wavelet denoising methods is usual (Mallat, 2009) in signal processing and the use of wavelets for the representation of GW signals has been mentioned in several LIGO/Virgo Collaboration articles (Abbott et al, 2017b, 2016b; Cornish and Littenberg, 2015). In our work we have used the discrete FIR approximation of Meyer wavelet; which has the properties of being symmetric, orthogonal and biorthogonal. More concretely, we have used the wavelet ‘dmey’ included in the package PyWavelets (pywt) in the PYTHON language (Lee et al, 2019). Having chosen a convenient lapse of time for the study, we perform the decomposition of the signals in terms of this wavelet basis and apply denoising methods (Mallat, 2009) to those coefficients; and then reconstruct the signal.

The denoised strains in the lapse of time of interest are shown in Figs. 2 and 3.

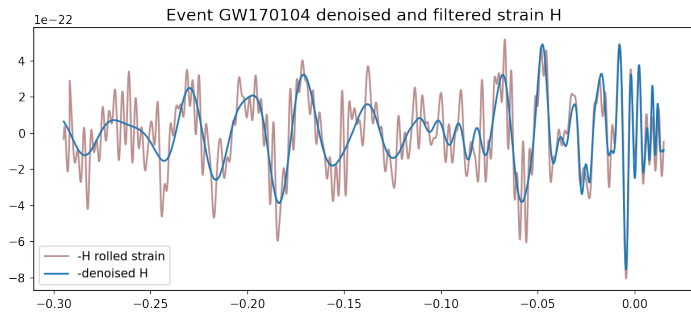


Fig. 2 Strain and denoised data for Hanford LIGO detector for GW170104 near the event time, with bandpass filter of [30,350]Hz.

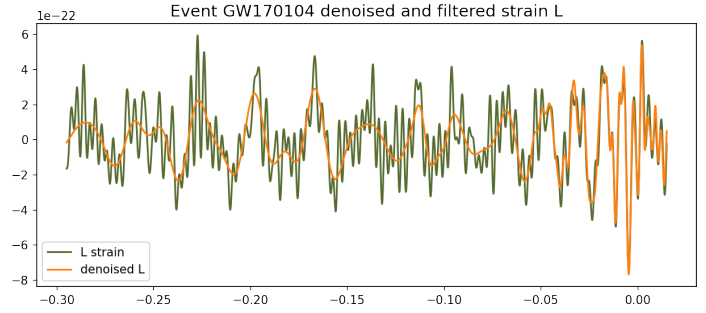


Fig. 3 Strain and denoised data for Livingston LIGO detector for GW170104 near the event time, with bandpass filter of [30,350]Hz.

The error in the denoised data depends on several factors and can not be perfectly calculated without knowing the precise value of the signal, as it is our case. We can at most give estimates of them based on the characteristics of the ambient present noise. We have limited some of the factors inherent in the calculation by an appropriate choice of the wavelet basis. Let us expand on this. The wavelet transform comes in a variety of versions and the analyst has to choose the framework that best suits the needs of the type of data under study. To begin with, wavelet transforms comes in continuous and discrete versions. We use continuous wavelet transforms to study the global behavior of the signal in the scalograms we present in the section 4. But for the detailed local analysis of the signal we use a discrete basis. There is a great variety of them; for our purposes we require the basis to be orthogonal, since it is important for us to preserve the energy of the system. Since ultimately we intend to make a decomposition of the signal in terms of its polarization modes, their phase behavior is also important for us, which is associated with the symmetry and biorthogonal (Mallat, 2009; Cohen et al, 1992) properties of the basis. By choosing the Discrete Meyer (FIR Approximation), mentioned above, we obtain all the desired properties for a wavelet basis; thus mitigating factors that could contribute to errors in the analysis. The crude estimate of the error is calculated from the local standard deviation of the difference between the strain and the denoised datum for each case; which we use. These are understood as upper bounds on the possible errors of the denoised data.

It should probably be emphasized that our techniques for denoising the strains do not assume the existence of the polarization modes; which is a completely different approach from the one mentioned in LIGO Scientific and Virgo Collaborations articles (Abbott et al, 2017b) on the use of wavelet analysis.

4 Study of the nature of the signals in the time-frequency domain

As part of the systematic analysis of the strains of an event is the study of the characteristics of the signal in the

time-frequency domain. It is then usual to study the spectrograms and scalograms of the strains. We have found that it is better to resort to scalograms for our purposes; which we show in Figs. 4 and 5.

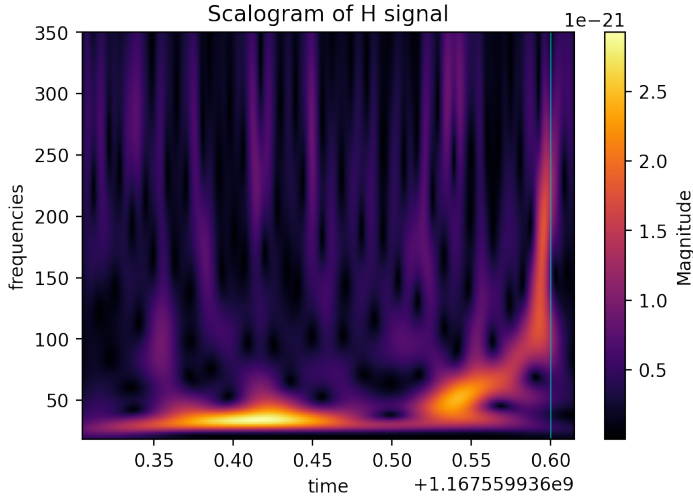


Fig. 4 Detail of the strain of LIGO detector H for GW170104 with a pass band of [30,350]Hz.

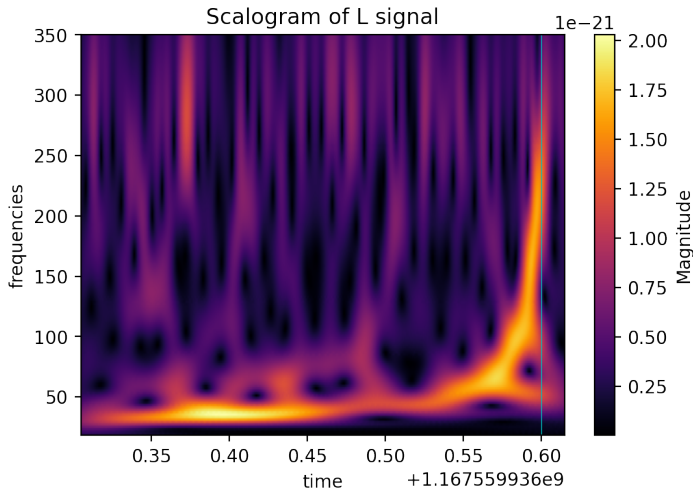


Fig. 5 Detail of the strain of LIGO detector L for GW170104 with a pass band of [30,350]Hz.

It is easy to observe a chirp like signal in both detectors. We have indicated with a vertical line an approximate chirp time.

5 Using a universal fitting chirp form for gravitational-wave polarization modes

Due to the chirp like nature of the signal, we study here the possibility of fitting the gravitational-wave polarization modes with a couple of universal chirp shape functions, that could handle a gross representation of the modes during the inspiral phase. In order to fit the observed data it is better to use the widest time range. For early times it is expected that a universal fitting form be good enough to perform the adjustment of parameters. In this work we choose the function $g(t) = 1/((t_f - t)^{p_a/4} + \epsilon_t^{p_a/4})$ for fitting the amplitude time dependence of the modes, and the function $\Phi(t) = -2\left(\frac{t_f - t}{5t_{ch}}\right)^{p_c/5/8} + \phi_f$ for fitting the phase time dependence of the modes. Then, we define mono-components polarization modes as:

$$P_+(t) = A_+ g(t) \cos(\Phi(t)), \quad (9)$$

and

$$P_\times(t) = A_\times g(t) \sin(\Phi(t)), \quad (10)$$

with adjustable parameters $[A_+, A_\times, \phi_f]$; while the other parameters $[t_f, p_a, \epsilon_t, t_{ch}, p_c]$ are fixed from the time frequency studies. Note that one can use eq. (61) for a fitting approximation of the signal w'_X in detector X . More concretely, we define the corresponding fitting signals

$$w'_X = B_{+X} g(t) \cos(\Phi(t)) + B_{\times X} g(t) \sin(\Phi(t)). \quad (11)$$

This expression however has a degeneracy among the parameters $[B_+, B_\times, \phi_f]$ that is treated below.

In order to determine the original $[A_+, A_\times]$ amplitudes we express w' in terms of the orientation angles for each detector; namely:

$$\begin{aligned} w'_H &= F_{+H0} P_+ + F_{\times H0} P_\times \\ &= B_{+H} g(t) \cos(\Phi(t)) + B_{\times H} g(t) \sin(\Phi(t)), \end{aligned} \quad (12)$$

and similarly

$$\begin{aligned} w'_L &= F_{+L0} P_+ + F_{\times L0} P_\times \\ &= B_{+L} g(t) \cos(\Phi(t)) + B_{\times L} g(t) \sin(\Phi(t)); \end{aligned} \quad (13)$$

from which one finds

$$B_{+H} = F_{+H0} A_+, \quad (14)$$

$$B_{\times H} = F_{\times H0} A_\times, \quad (15)$$

$$B_{+L} = F_{+L0} A_+, \quad (16)$$

$$B_{\times L} = F_{\times L0} A_\times. \quad (17)$$

Then, we have two equations for the single value of A_+ and another couple of equations for A_\times which should help us in determining the three angles (δ, α, ψ) . But we should

also use the combination $A^2 \equiv A_+^2 + A_\times^2$, due to its transformation properties. More concretely, we can look for the zeros of

$$J_{HL}(\delta, \alpha, \psi) = A_H^2 - A_L^2, \quad (18)$$

which is expected to have multiple minima on the celestial sphere.

Note also that one has the relations

$$B_{+H}F_{+L0} = B_{+L}F_{+H0}, \quad (19)$$

and

$$B_{\times H}F_{\times L0} = B_{\times L}F_{\times H0}. \quad (20)$$

So that we can study the zeros of

$$C_+(\delta, \alpha, \psi) = B_{+H}F_{+L} - B_{+L}F_{+H}, \quad (21)$$

and

$$C_\times(\delta, \alpha, \psi) = B_{\times H}F_{\times L} - B_{\times L}F_{\times H}, \quad (22)$$

or better the minima of their squares. Then, for each choice of ψ we also study the minima of

$$N(\delta, \alpha, \psi) = C_+^2 + C_\times^2, \quad (23)$$

in terms of the location angles; with the difficulty that the minimum of one is washed by the other. Alternatively, we can study the maxima of

$$N(\delta, \alpha, \psi) = \frac{1}{C_+^2} + \frac{1}{C_\times^2}; \quad (24)$$

where each minimum of $C_{+, \times}$ contributes independently.

We will use as initial measure the function

$$M_i = \frac{1}{\sqrt{N}} = \frac{1}{\sqrt{C_+^2 + C_\times^2}}; \quad (25)$$

where the location would be indicated by the maximum values.

The results of fitting a universal chirp form for the polarization of the GW to the denoised signals are shown in Figs. 6 and 7.

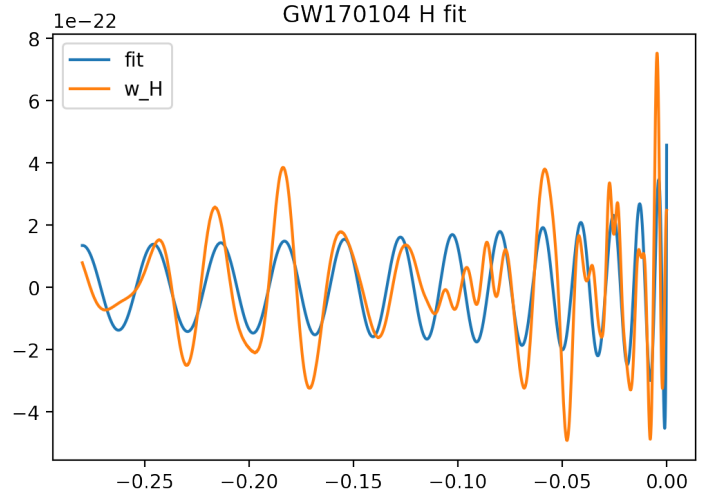


Fig. 6 Fitting result to the denoised signal H.

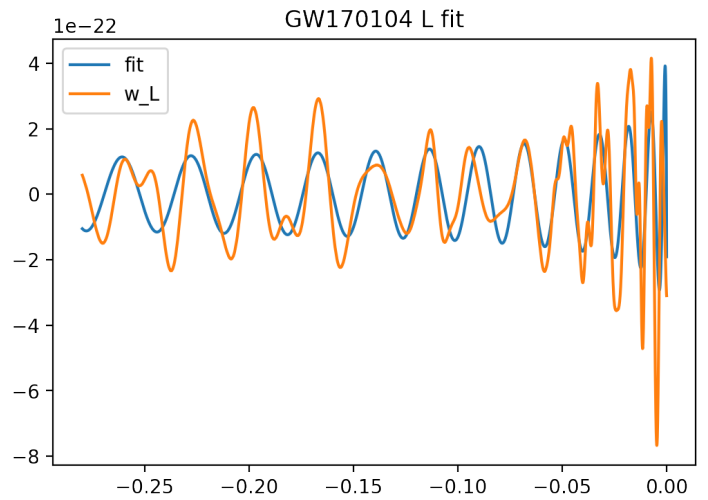


Fig. 7 Fitting result to the denoised signal L.

It is obvious that this is a gross approximation to the signals; but the remarkable result is that even with this universal fitting chirp forms we can obtain excellent results; as shown below.

It is probably worthwhile to comment on the role of the angle ψ . At this stage ψ is a hyperparameter which is adjusted by using the measure N so that the crossing appears on the delay ring. Since our intention is to present a procedure to localize the source, and to reconstruct the spin-2 polarization modes, we are trying to obtain these goals as far as we can without entering into the detail astrophysical description of the source system; that is, in terms of inclination of the orbital plane and other parameters. For this reason we do not intend in this article to relate our ψ to the detailed description of the source. But with a more accurate prescription of the proposed polarization modes, this procedure would employ a ψ that would probably give

a good first estimate to relate to the natural GW base as described in terms of the source orbit parameters (Poisson and Will, 2014).

6 Injected signals from synthetic spin-2 polarization modes

6.1 Injected signals and denoised reconstruction

In this section we apply the L2D+PMR procedure to the case of injected signals that have been generated from spin-2 polarization modes at different locations in the celestial sphere and with distinct polarization frames. To incorporate realistic noise conditions, we perform signal injections on the strains from the GW170104 event after subtracting the corresponding denoised signals. This process allows us to construct ten synthetic variations of the event, which we refer to as GW170104synth. To evaluate the impact of this subtraction, we compare the H and L strains before and after removing the denoised signals w . The difference is illustrated through the OM measure Λ introduced in Moreschi (2024), as shown in Fig. 8.

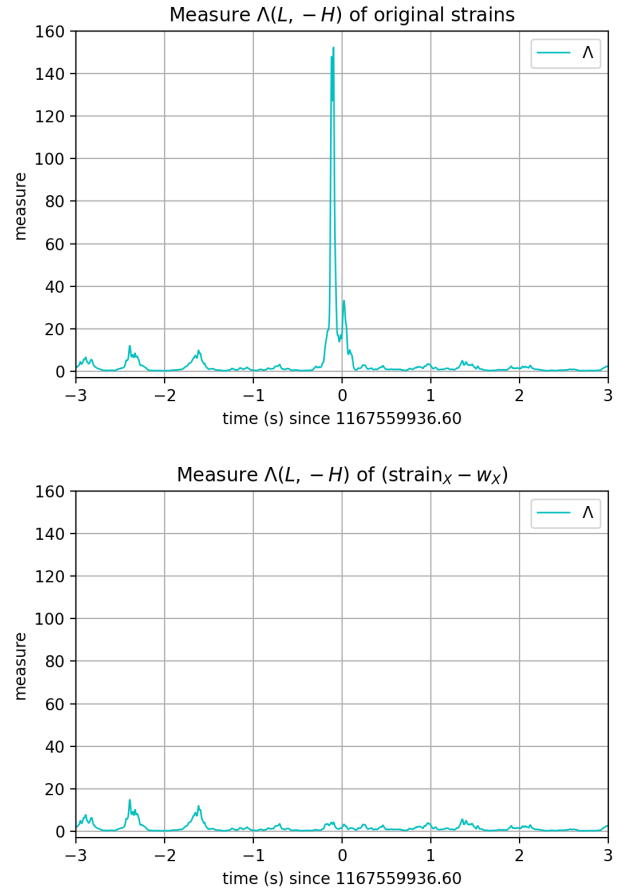


Fig. 8 On the top graph, the values of the measure Λ close to the reference event time for the original filtered strains of GW170104, and on the bottom for the strains after the subtraction of the denoised signals w from the spin-2 polarization modes. The residual is ambient noise.

As shown in Fig. 8, the comparison between the H and L strains of GW170104 after subtracting the denoised signals reveals no significant coincidence within the studied time window. It must be stressed that these graphs are generated with the initial bandpass filter in the range $[27,1003]$ Hz; that is, the injected signals have the intrinsic initial noise.

To complement this observation, we also present the Amplitude Spectral Density (ASD) graphs of these strains after subtraction in Fig. 9, which provide insight into the spectral characteristics of the remaining noise.

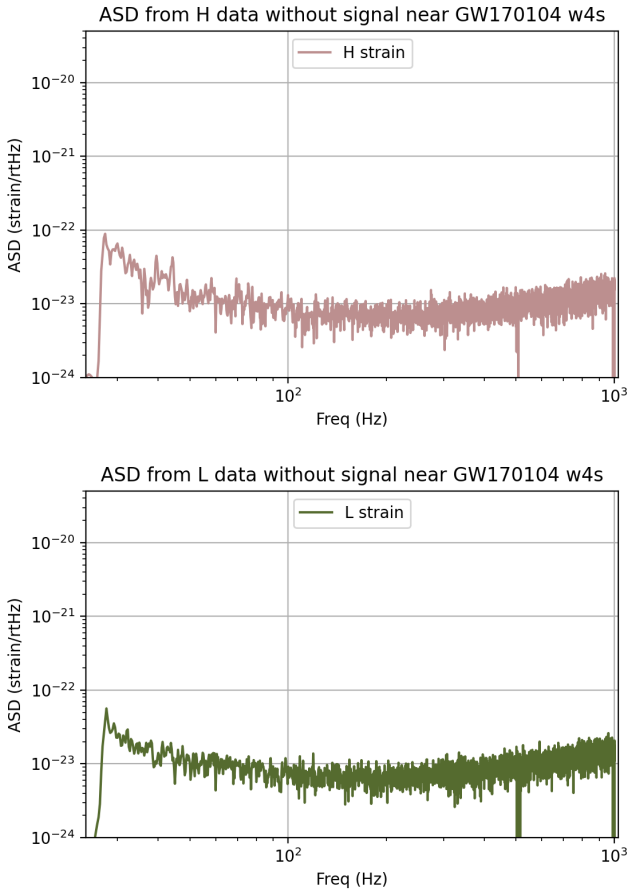


Fig. 9 On the top graph, the ASD of strain H of the 22s around the time of the event GW170104, and on the bottom graph the corresponding ASD for the L strain.

In Fig. 9 one can see the nature of the state of the noise for the event GW170104, in a lapse of time of 22s centered at the event time. This is of course after we have applied the preprocessing filtering techniques (Moreschi, 2019).

For reasons of time and space we present in this occasion ten simulations. Since our methods do not rely on the astrophysical information of the signal, but rather on the spin-2 behavior, we consider for this purpose a signal, generated by very simple polarization modes; which details are described in appendix L. They correspond to a post-Newtonian (Jaranowski and Krolak, 2009; Poisson and Will, 2014) system with radiation reaction as described by Peters (1964) with initial 0.35 eccentricity. We study ten different locations of this signal on a different delay ring corresponding to a time difference of 0.005737s. We denote the cases from 1 to 10. The polarization frames were chosen at random from 10 different options, for each case by taking $\Delta\psi = 0, 0.6891, 0.7854, 0.6108, 0.1745, 0.4363, 0.3490, 0.0873, 0.5236$ and 0.2618 respectively; while the relative amplitudes were chosen as $A_{ch} = 7 \times 10^{-22}$. With these choices we intend to cover a variety of situations one could encounter in the location and reconstruction tasks.

In order to verify the denoising procedure quantitatively we here calculate the correlation coefficient (Ferguson, 1967; Helstrom, 1975; McDonough and Whalen, 1995) between the two signals in terms of the natural inner product as described in Moreschi (2024).

The comparison of the original synthetic signals with the corresponding denoised signals extracted from the strains with the noise of the GW170104 event are shown in Figs. 10–19.

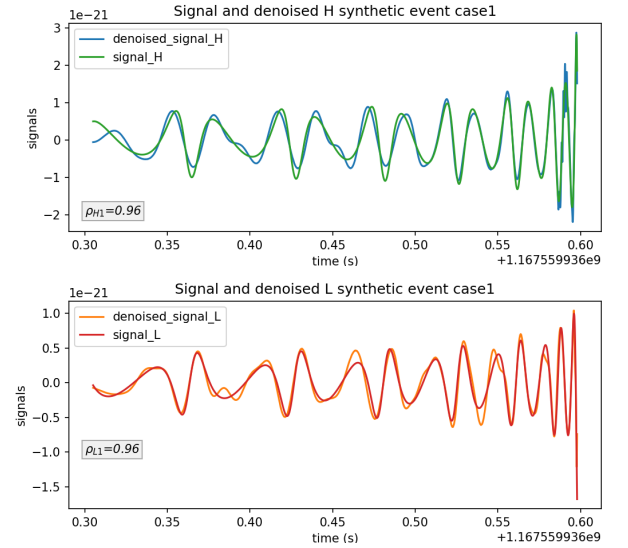


Fig. 10 Top panel, comparison of original synthetic signal_H with the extracted denoised signal from H strain with the noise of the GW170104 event. In the bottom panel the corresponding graphs for L. The inset shows the value of the correlation coefficient for both curves.

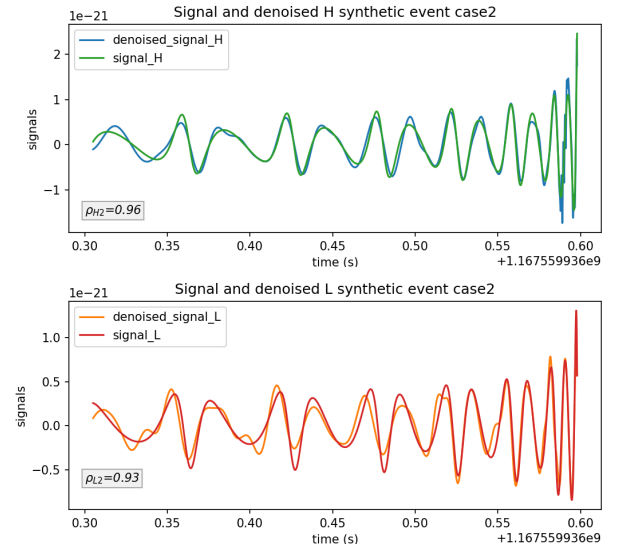


Fig. 11 Top panel, comparison of original synthetic signal_H with the extracted denoised signal from H strain with the noise of the GW170104 event. In the bottom panel the corresponding graphs for L. The inset shows the value of the correlation coefficient for both curves.

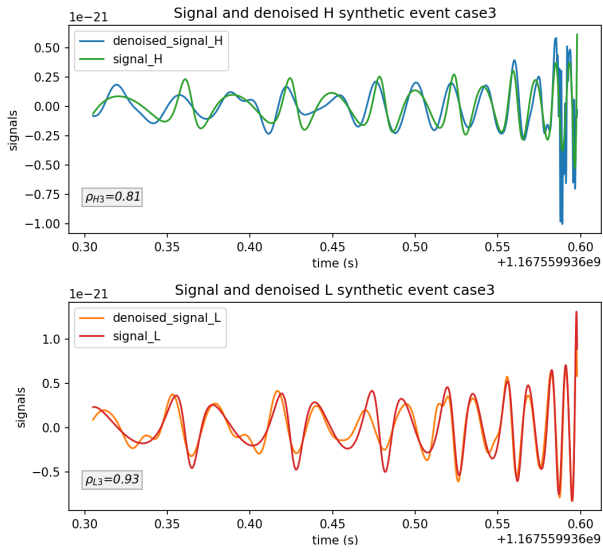


Fig. 12 Top panel, comparison of original synthetic signal_H with the extracted denoised signal from H strain with the noise of the GW170104 event. In the bottom panel the corresponding graphs for L. The inset shows the value of the correlation coefficient for both curves.

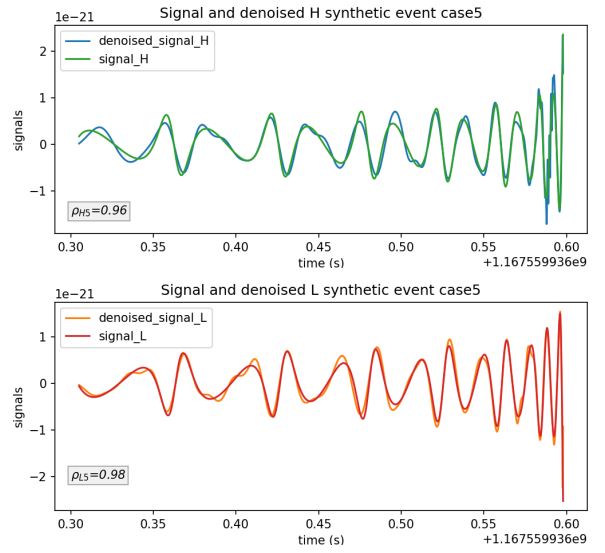


Fig. 14 Top panel, comparison of original synthetic signal_H with the extracted denoised signal from H strain with the noise of the GW170104 event. In the bottom panel the corresponding graphs for L. The inset shows the value of the correlation coefficient for both curves.

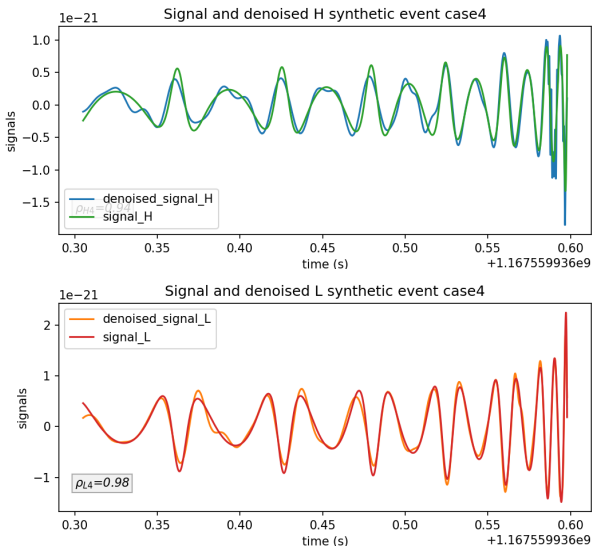


Fig. 13 Top panel, comparison of original synthetic signal_H with the extracted denoised signal from H strain with the noise of the GW170104 event. In the bottom panel the corresponding graphs for L. The inset shows the value of the correlation coefficient for both curves.

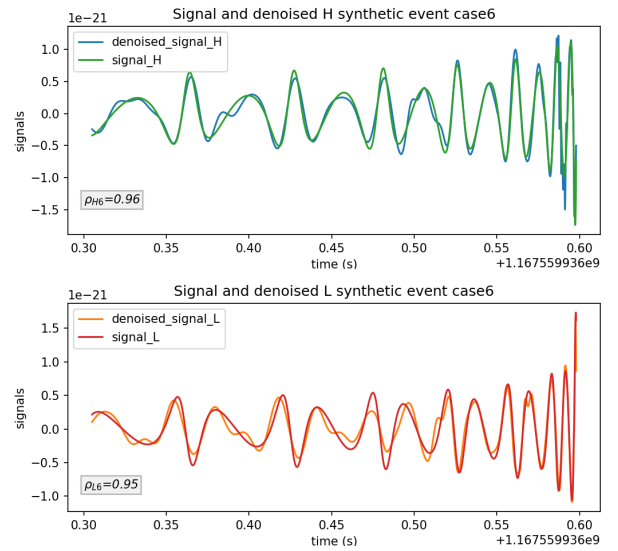


Fig. 15 Top panel, comparison of original synthetic signal_H with the extracted denoised signal from H strain with the noise of the GW170104 event. In the bottom panel the corresponding graphs for L. The inset shows the value of the correlation coefficient for both curves.

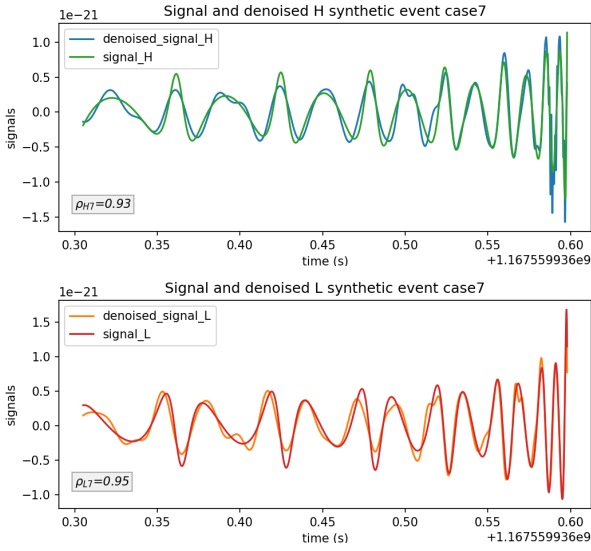


Fig. 16 Top panel, comparison of original synthetic signal_H with the extracted denoised signal from H strain with the noise of the GW170104 event. In the bottom panel the corresponding graphs for L. The inset shows the value of the correlation coefficient for both curves.

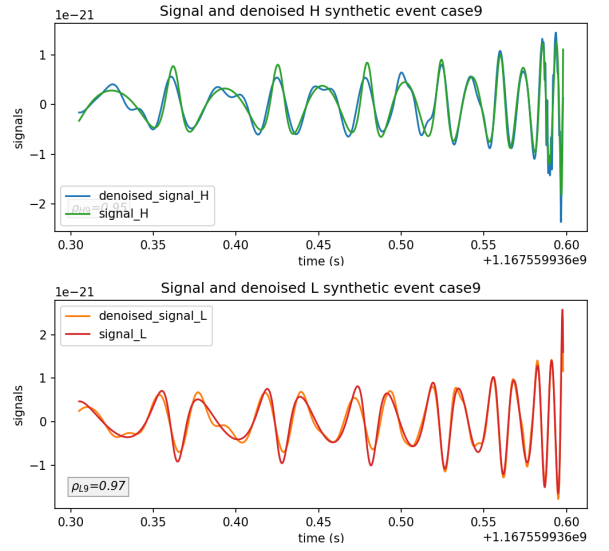


Fig. 18 Top panel, comparison of original synthetic signal_H with the extracted denoised signal from H strain with the noise of the GW170104 event. In the bottom panel the corresponding graphs for L. The inset shows the value of the correlation coefficient for both curves.

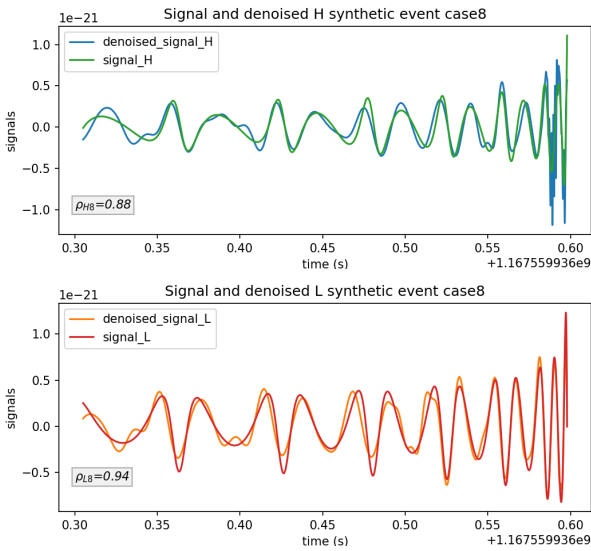


Fig. 17 Top panel, comparison of original synthetic signal_H with the extracted denoised signal from H strain with the noise of the GW170104 event. In the bottom panel the corresponding graphs for L. The inset shows the value of the correlation coefficient for both curves.

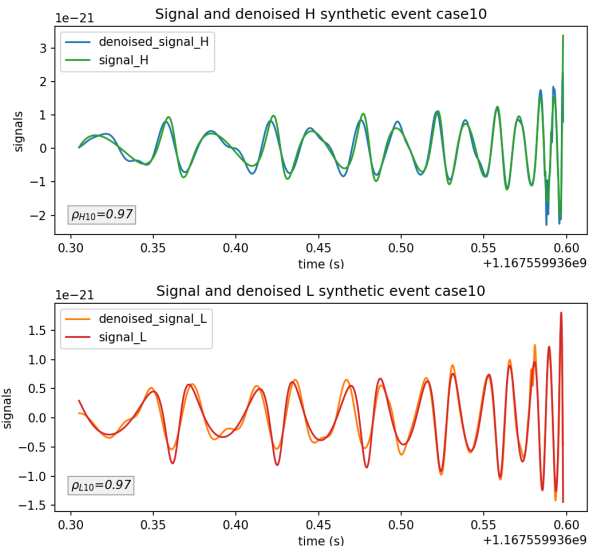


Fig. 19 Top panel, comparison of original synthetic signal_H with the extracted denoised signal from H strain with the noise of the GW170104 event. In the bottom panel the corresponding graphs for L. The inset shows the value of the correlation coefficient for both curves.

It can be seen that the denoising techniques make an excellent job in finding the signals in the strains with real noise, in both detectors. This can be observed from the behavior of the curves in these graphs; but it can also be reflected from the results in the calculation of the correlation coefficients for the pair of curves whose histograms are presented in Fig. 20.

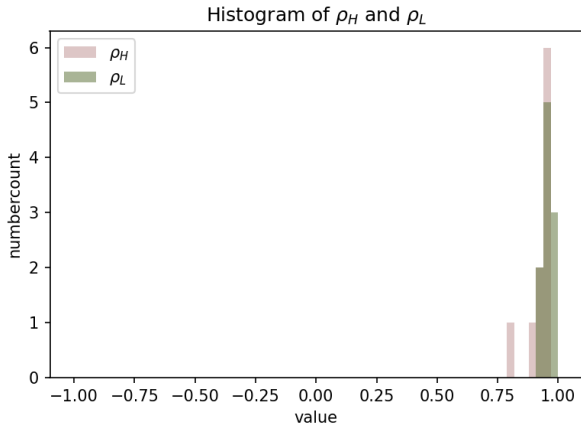


Fig. 20 Histograms of ρ_H and ρ_L superimposed. The darker regions indicates same covering for both graphs.

Although the sample size is relatively small, Fig. 20, which presents histograms of ρ_H and ρ_L , shows that their values are predominantly concentrated near their respective maxima. This indicates that the denoising techniques effectively recover very well the original signal across all tested scenarios.

To see other approaches for denoising and the reconstruction of gravitational-wave signals and their result on injected simulated waveform please see [Bacon et al \(2023\)](#); [Chatterjee and Jani \(2024\)](#).

6.2 Localization

It is important to emphasize that localization based on time delay studies is the first and most fundamental method available in gravitational-wave observations. As evident from equation 1, the presence of time delays between observatories is essential for the study of the wave’s content across multiple detectors.

However, the time delay between two observatories does not define a precise triangular localization but rather a delay ring in the sky. Therefore, the first estimate for the source’s location is always a region surrounding this delay ring.

Given this, any additional localization method is expected to yield results that are consistent with and situated near the delay ring. In this study, we construct a Gaussian region around the nominal delay ring, providing an estimate of the probability distribution of the sky localization based solely on time delay considerations.

In methods where probability density maps are available, constructing confidence level regions is straightforward. However in our case, we do not have probability density maps, nor have we estimated any from our approach. Instead, we construct sky maps based on measures derived from observational noisy data after appropriate processing. To estimate confidence level regions, we apply Chebyshev’s inequality ([Casella and Berger, 2002](#)), treating our measure

M_i as an indicator of a signal within a random variable process. This approach allows us to define confidence regions in a rigorous manner, even in the absence of conventional probability distributions. In this way, high values of M_i give us indications of a signal, as compared with respect to the mean value μ in units of the standard deviation σ . So for example to estimate a 0.9 region, one looks for the boundary value $v_0 = \mu + t\sigma$; with $\frac{1}{t^2} = 0.1 = 1 - 0.9$. It should be noted that M_i is positive definite, and so v_0 is greater than μ . The difficulty with this estimate for the boundary value is that although M_i is giving us a signal over some noise; it does not provide a single signal, but also yields several phantom and additional non physical maxima. This has as a consequence, that the sample mean value overestimates the noise mean value, and the sample standard deviation overestimates the noise standard deviation. To cope with this situation, we could select a diminishing parameter c_{90} that, in order to deal with the phantom repetition, should be ≤ 0.5 . In the previous discussion, we did not explicitly account for the fact that we already have an initial estimate of the probability distribution for the source’s sky localization; this estimate is provided by the Gaussian regions. These regions serve as a crucial starting point, refining our understanding of the source’s potential location. In the following analysis, we incorporate this information to further improve our localization accuracy.

The need for a diminishing factor is naturally resolved if we instead use the ultimate measure $M_u = \{|G_{\text{ring}} * M_i|\}$; This measure represents the normalized product of the Gaussian distribution, interpreted as a probability estimate, associated with the delay ring (as shown in Fig. 1) and the initial measure M_i . By incorporating this approach, we ensure a more refined and reliable localization estimate. It is important to note that the more precise measure M_u naturally emerges from the inferable knowledge about the source location derived from time delay considerations. In this formulation, M_u effectively suppresses phantom signals when they are positioned away from the delay ring. As a result, we can apply Chebyshev’s inequalities directly, without requiring any additional corrective factors.

The final M_u 0.9 region constructed from the direct application of the Chebyshev inequality to case 1 is shown in Fig. 21.

GW170104synth combined 0.9 confidence level region

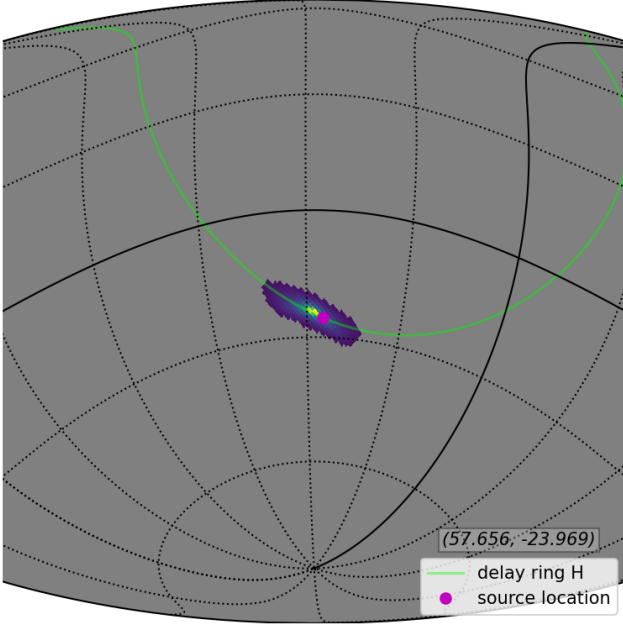


Fig. 21 This Mollweide view, shows the final 0.9 region for the GW170104synth synthetic signal case 1. The magenta circle indicates the position of the synthetic signal. The two numbers between parentheses denote the preferred central position as longitude and latitude.

GW170104synth combined 0.9 confidence level region

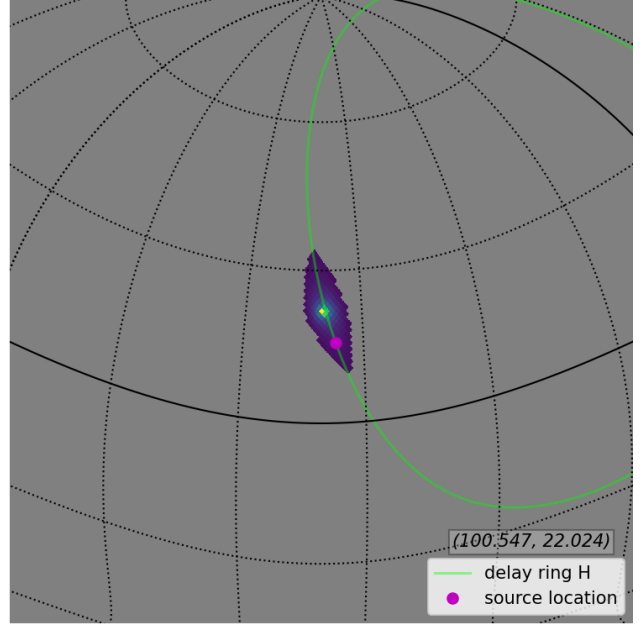


Fig. 23 This Mollweide view, shows the final 0.9 region for the GW170104synth synthetic signal case 3. The magenta circle indicates the position of the synthetic signal. The two numbers between parentheses denote the preferred central position as longitude and latitude.

The final 0.9 regions for the other cases 2–10 are shown in Figs. 22-30.

GW170104synth combined 0.9 confidence level region

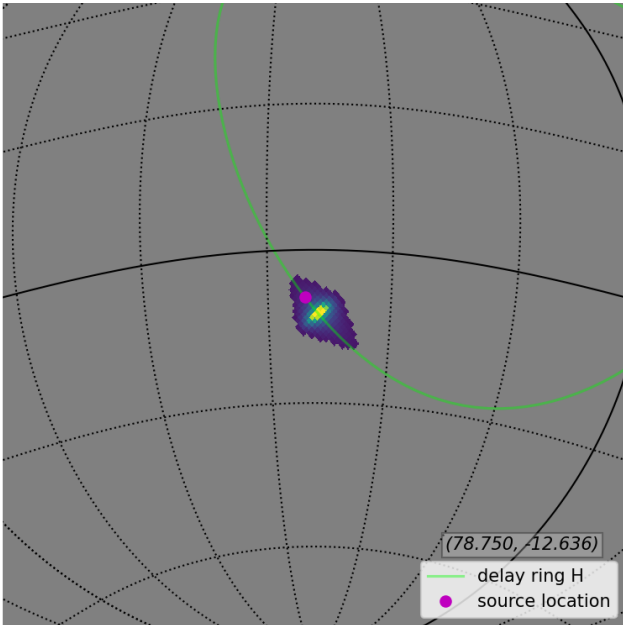


Fig. 22 This Mollweide view, shows the final 0.9 region for the GW170104synth synthetic signal case 2. The magenta circle indicates the position of the synthetic signal. The two numbers between parentheses denote the preferred central position as longitude and latitude.

GW170104synth combined 0.9 confidence level region

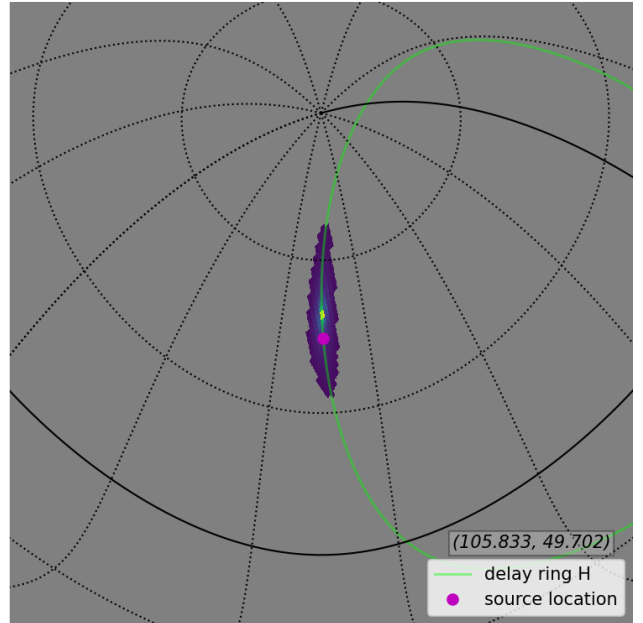


Fig. 24 This Mollweide view, shows the final 0.9 region for the GW170104synth synthetic signal case 4. The magenta circle indicates the position of the synthetic signal. The two numbers between parentheses denote the preferred central position as longitude and latitude.

GW170104synth combined 0.9 confidence level region

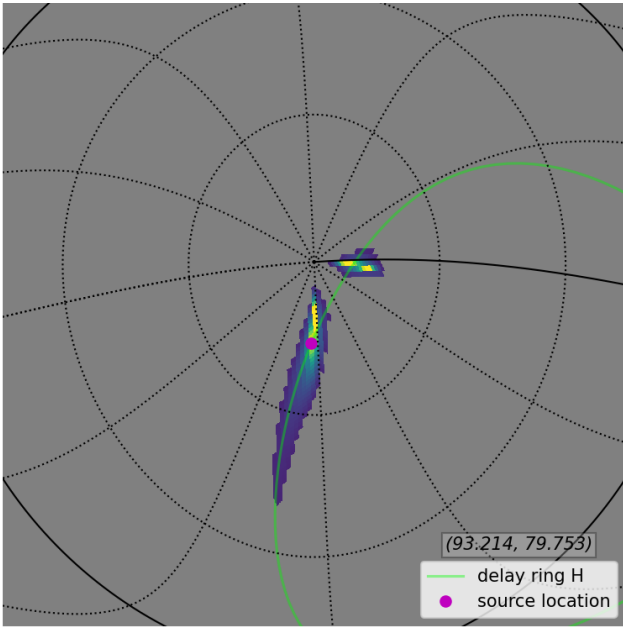


Fig. 25 This Mollweide view, shows the final 0.9 region for the GW170104synth synthetic signal case 5. The magenta circle indicates the position of the synthetic signal. The two numbers between parentheses denote the preferred central position as longitude and latitude.

GW170104synth combined 0.9 confidence level region

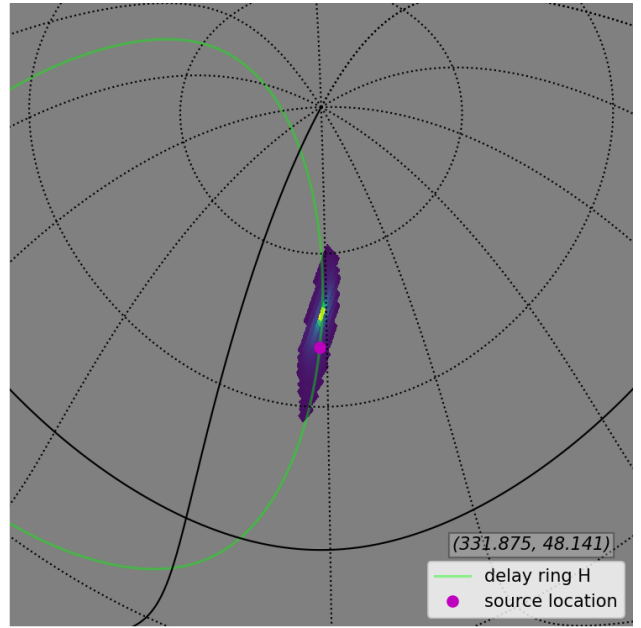


Fig. 27 This Mollweide view, shows the final 0.9 region for the GW170104synth synthetic signal case 7. The magenta circle indicates the position of the synthetic signal. The two numbers between parentheses denote the preferred central position as longitude and latitude.

GW170104synth combined 0.9 confidence level region

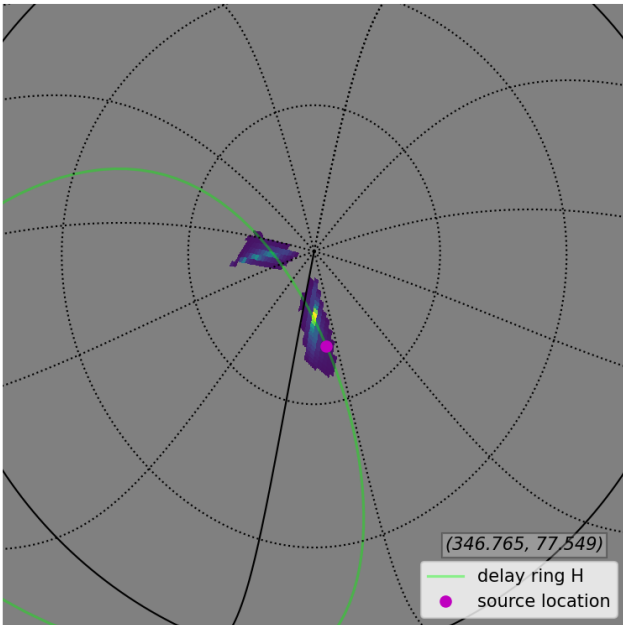


Fig. 26 This Mollweide view, shows the final 0.9 region for the GW170104synth synthetic signal case 6. The magenta circle indicates the position of the synthetic signal. The two numbers between parentheses denote the preferred central position as longitude and latitude.

GW170104synth combined 0.9 confidence level region

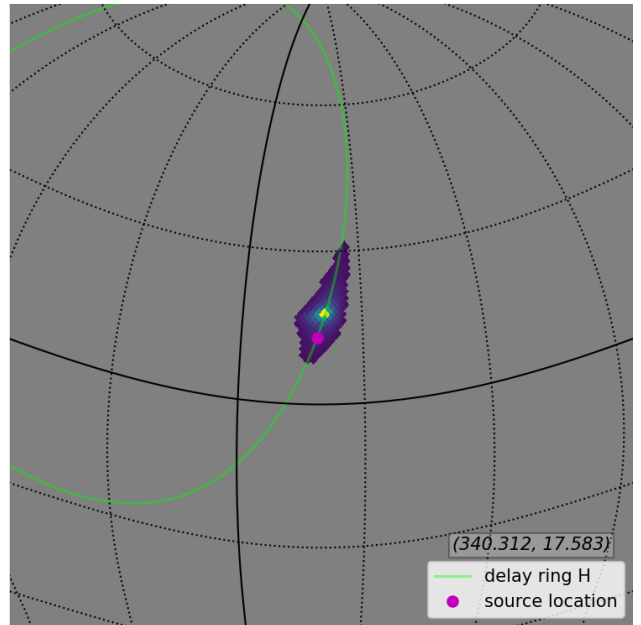


Fig. 28 This Mollweide view, shows the final 0.9 region for the GW170104synth synthetic signal case 8. The magenta circle indicates the position of the synthetic signal. The two numbers between parentheses denote the preferred central position as longitude and latitude.

GW170104synth combined 0.9 confidence level region

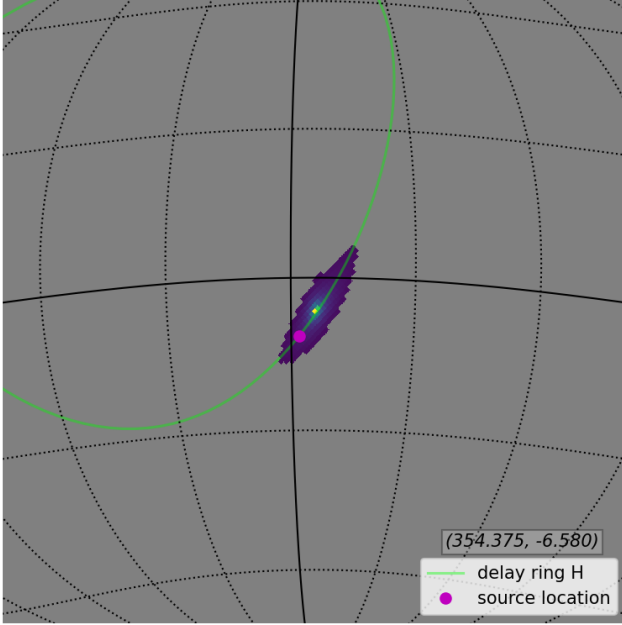


Fig. 29 This Mollweide view, shows the final 0.9 region for the GW170104synth synthetic signal case 9. The magenta circle indicates the position of the synthetic signal. The two numbers between parentheses denote the preferred central position as longitude and latitude.

GW170104synth combined 0.9 confidence level region

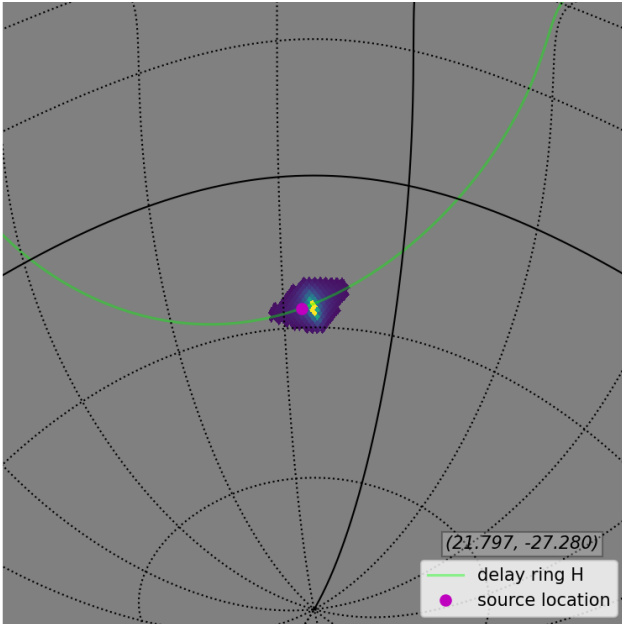


Fig. 30 This Mollweide view, shows the final 0.9 region for the GW170104synth synthetic signal case 10. The magenta circle indicates the position of the synthetic signal. The two numbers between parentheses denote the preferred central position as longitude and latitude.

The irregular shapes and saw type edges are due to the discretization effects on the sphere.

The area of the 0.9 regions in square degrees for each case are 248, 193, 165, 183, 410, 174, 196, 169, 175 and 162 respectively. The actual errors in the preferred pixel's position and the exact location of the synthetic sources are in all cases few degrees; which shows reasonable precision properties of this localization method.

There are some works studying theoretical predictions on the precision of localization for gravitational wave detectors. For example in Fairhurst (2009, 2011), the author examines the accuracy of source localization using a network of detectors by analyzing how gravitational-wave detectors measure transient signals based solely on timing information at each site. However, these studies do not take into account the polarization mode content of the GW. As a result, we anticipate that our method will yield different uncertainty estimates due to its incorporation of polarization mode information. Instead in Wen and Chen (2010) the authors dealt with the problem of obtaining general geometrical expressions for the angular resolution of an arbitrary network of interferometric GW detectors when the arrival time of a GW is unknown; which is different from our case because we use the delay time information in our procedure. In any case, in this last reference they propose that for the two LIGO detector case one would expect an error of about 5° ; which is consistent with our results that we have just presented.

6.3 Reconstruction of the spin-2 polarization modes

Regarding the measurement of the polarization modes, we show in Figs. 31 and 32 the reconstructed polarization modes (in blue) along with the exact injected version (in green), that were used to build the synthetic signal at the new source position for the case 1.

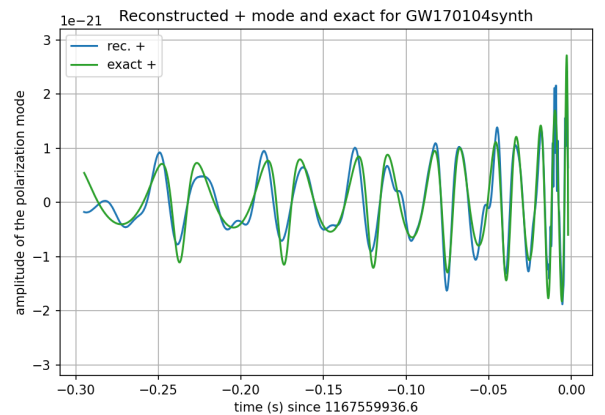


Fig. 31 Reconstructed + polarization mode and exact initial corresponding mode; used in the injected signal for first case.

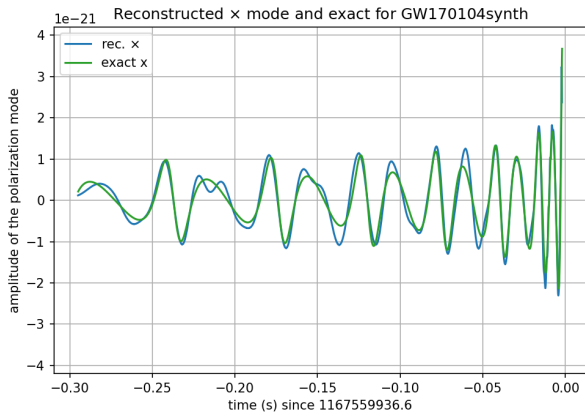


Fig. 32 Reconstructed \times polarization mode and exact initial corresponding mode; used in the injected signal for first case.

It can be noted that the slight error in the determination of the sky localization of the synthetic source does not preclude an excellent reconstruction of the original polarization modes.

7 Localization of GW170104

By ‘localization’ we mean the sky localization, that is, the celestial position of the source.

The result of our procedure for the localization of event GW170104 is presented in Fig. 33.

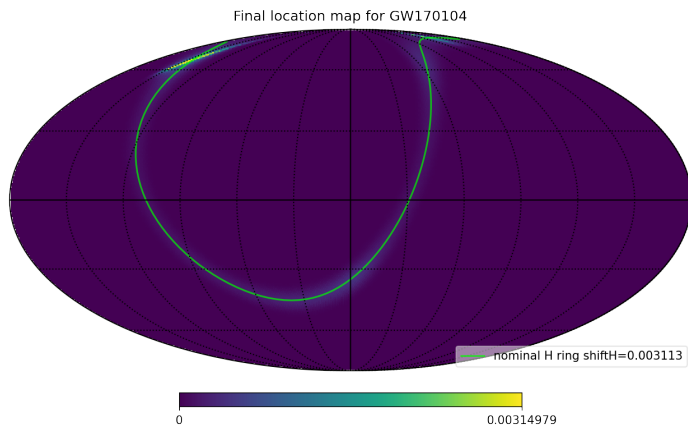


Fig. 33 Final sky localization for the source of the GW170104 event, where one can see a signal in the northern east part of the nominal ring.

This final location is obtained from the measure M_u described above. The preliminary location, is shown in Fig. 52 in appendix G.

To manipulate and show data on the celestial sphere we use the PYTHON package healpy employing 49152 pixels for the sphere. In our approach we do not use probabilities, but

instead we use measures on the sphere (M_u) whose maximum indicates the location of the source in the sky. We have not related this function to any probability distribution. For this reason, we estimate regions associated to level of significance using the Chebyshev inequality (Casella and Berger, 2002) to our measure. Choosing a level of significance $\alpha = 0.1$, we can select the region in the sky; where this criteria is satisfied, and so we characterize the confidence level region of $\gamma = (1 - \alpha) = 0.9$. The final region of interest at the 0.1 level of significance, is obtained from M_u ; which is shown in Fig. 34. Further discussion is presented in section 6; but we should probably note here that the meaning or our confidence level region, based on the values of a measure on the sphere (where the location is indicated by its maximum values over noise) is different from the notion of confidence area (or region) defined on the values of a probability density function.

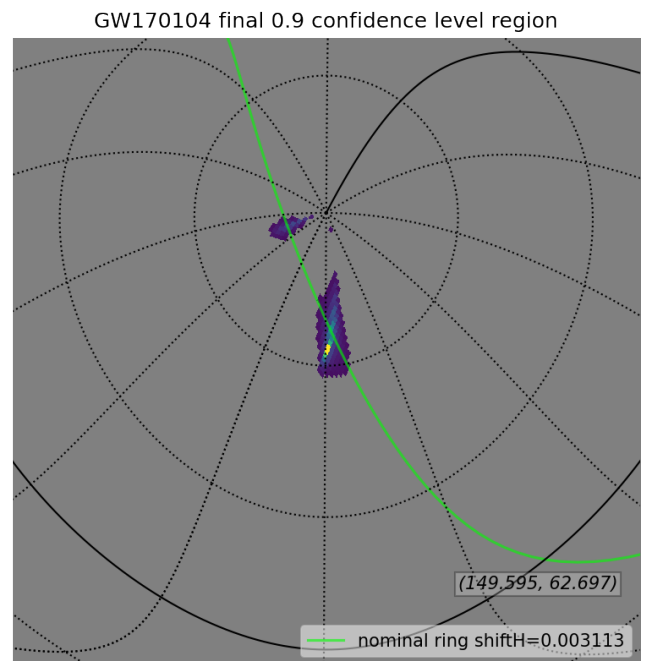


Fig. 34 Final sky localization for the source of the GW170104 event, with 0.9 confidence level region of measure M_u . The two numbers between parentheses denote the preferred central position as longitude and latitude.

The measure shown in Fig. 34 has maximum at celestial coordinates, longitude and latitude, (150, 63) degrees; and the area covered by pixels with a confidence level of 0.9 or higher is 142 square degrees. The global maximum is found in a single distinct pixel.

Our final localization is close to one of the local maxima communicated by the LIGO Scientific Collaboration (LIGO, 2017) that we reproduce in Figs. 35 and 36. Getting into more detail, it can be seen that both LIGO approaches yield two local maxima on the delay ring; the absolute maximum in the northeastern sector and the second local maximum in the southwest sector. The procedure we are presenting here

is very different from the LIGO approaches and so probably this is the main reason that our result does not coincide exactly with their absolute maximum, although our maximum is within the region of their main maximum area. At this time, studying a single event one can not state which of these approaches is more accurate; mainly because for this event there are no electromagnetic counter parts. We should not compare the surface area of our confidence level region derived from a measure, with the confidence limit regions defined by probability density functions as previously mentioned; since they have fundamentally different meaning. It would be convenient to perform further studies to clarify these issues. To address this, we plan to apply our procedure to a diverse set of real gravitational-wave events in future analyses.

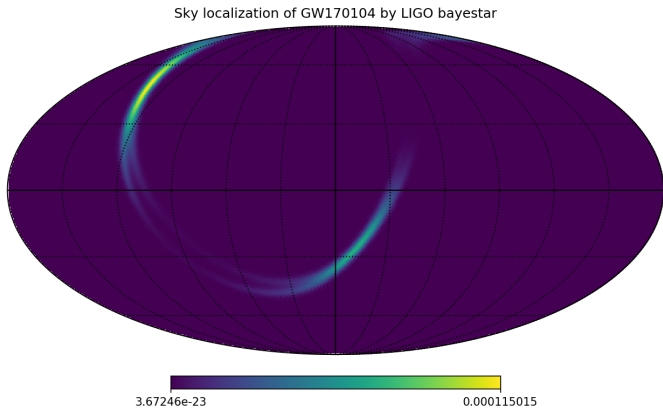


Fig. 35 Sky localization from LIGO team with Bayestar method.

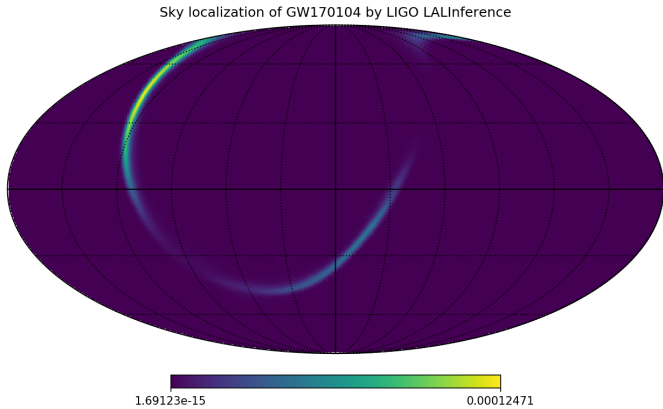


Fig. 36 Sky localization from LIGO team with LALInference method.

It is worth highlighting that in order to discuss the polarization mode content of a GW one needs to refer to a frame. In the next section we present the reconstructed polarization modes in terms of the basis obtained in the localization

procedure; but later in appendix K we also present the PMs in other frames related by a differential polarization angle $\Delta\psi$.

8 Reconstruction of the spin-2 polarization modes of GW170104

In the previous section we have presented the results on the localization of the source. Although the 0.9 region covers several square degrees, our measure has maximum at a single pixel; which we take as the position of the source for this part of our work. Then, knowing the localization in the celestial sphere of the source and applying denoising techniques as explained above we can perform the reconstruction of the PMs which we show in Fig. 37.

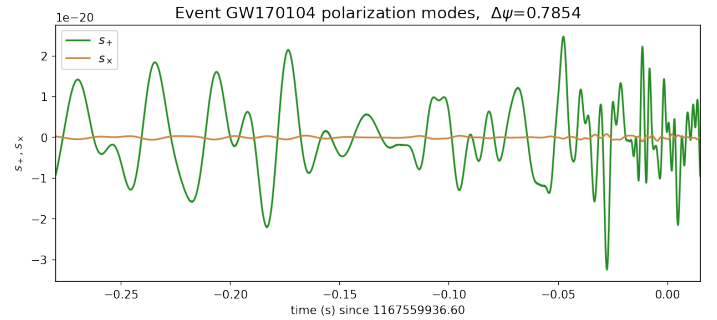


Fig. 37 Polarization modes + and × close to the reference time of the GW170104 event.

The graph in Fig. 37 shows that the × component is significantly smaller than the + component; although small variations in the × component remain visible. This demonstrates that both observatories recorded nearly identical spin-2 polarization mode components, and that the selected polarization frame happened to be one in which this effect is clearly observable.

It is noteworthy that the time series for s_+ exhibits an irregular shape that does not resemble the denoised signals shown in Figs. 2 and 3 which more closely match expected chirp-like signals. To understand this behavior, it is important to recognize that in cases where one detector has essentially recorded the negative of the signal recorded by the other detector, the algebraic reconstruction of polarization modes involves a subtraction between both signals, as demonstrated by the equations in Section 2. Specifically, we have verified that the factors $F_{\times E}$ and $F_{\times D}$ have opposite signs at the source location, and similarly, the factors F_{+E} and F_{+D} also have opposite signs at this location. This is expected when the signals at the observatories are anti-correlated and consequently results in cancellation of both signals during polarization mode calculation. This property is not a limitation of our procedure but rather a general characteristic of the algebra involving data from two observatories, as derived from eq. 1. We therefore interpret the

preceding time series for s_+ as exhibiting a high noise contribution, where the signal-to-noise ratio is insufficient to allow physically meaningful reconstruction of the polarization modes (PMs). Consequently, one expects significantly better results for cases where the source localization produces signals at the two observatories that are less strongly (anti)correlated.

In any case, there are no other comparable explicit reconstruction of the polarization modes $+$ and \times of a GW signal in the literature, as those shown with the time series in Fig. 37 close to the reference time of the GW170104 event. The subject of estimating errors for the reconstructed polarization modes for these special cases of great correlation between the signals of the observatories is complex and deserves a specific study, at present we concentrate in the presentation of the results of applying this procedure to this event and postpone for future works the study of additional contributions to errors due to correlation of the signals.

We however carryout first estimates of the error for the spin-2 polarization modes, using the information of the denoised signals, which are presented in Fig. 38. In order to check that the polarization modes behave as spin-2 quantities, we introduce in appendix K the calculation of the $+$ and \times PMs for the frames with $\Delta\psi = 0, \frac{\pi}{16}, \frac{2\pi}{16}, \frac{3\pi}{16}$; and we also calculate the consistency behavior of the PMs for $\Delta\psi = \frac{\pi}{4}$ with the $\Delta\psi = 0$ frame.

An estimate of the possible errors in the denoised data, can be calculated from the local standard deviation of the difference between the strain and the denoised datum for each case; carried out on an appropriate window length. Let us call this upper bound estimate σ_{X-w_X} ; where we use X to denote the strain of a detector and w_X its denoised signal.

When performing the reconstruction of the polarization modes, we use linear combinations of the denoised signals, of the form $P = aX + bY$. So that to estimate the possible error in their calculation we can apply the previous construction, and use the relation $\sigma_P^2 = a^2\sigma_{X-w_X}^2 + b^2\sigma_{Y-w_Y}^2 + 2ab\text{cov}(X-w_X, Y-w_Y)$ to estimate them; where cov means covariance.

In Fig. 38 we show the graphs of the polarization modes with their respective estimated error bands.

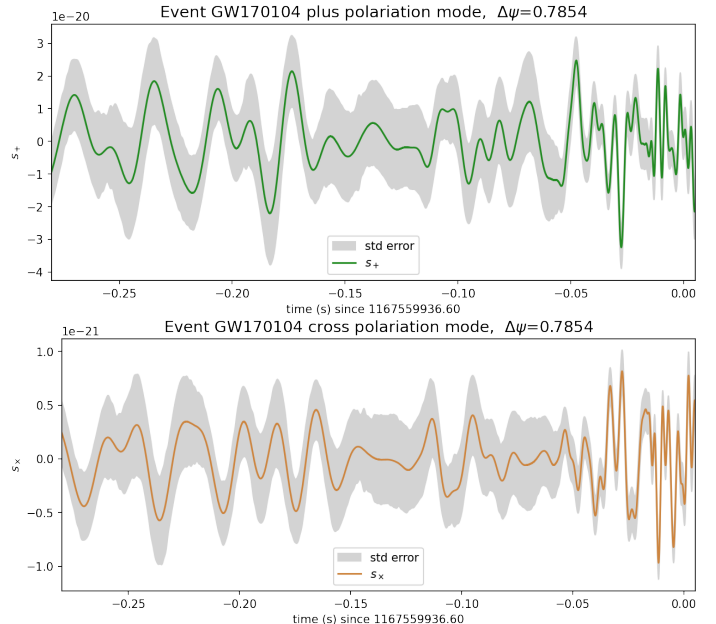


Fig. 38 Polarization modes of the event GW170104 for $\Delta\psi = 0.7854$ with estimated error bands, in the region close to the nominal event time.

The calculation for the time series polarization errors presented above provides estimates based on the statistics of the denoised signals. The differences between both graph is due to the way the detector pattern functions contribute to the final expressions. We expect that these error estimates will increase when a detailed treatment of the high correlation between signals from both observatories is taken into account; a study that we defer to future work

9 Complete reconstruction of the signal in terms of the spin-2 polarization modes for GW170104

We study here the situation in which the GW signal is decomposed only in terms of the spin-2 polarization modes. From the decomposition of the signal in terms of these PMs and having obtained previously the sky localization of the source, we can use a similar equation to (1) to reconstruct the signal of the GW at each detector. Explicitly, we define the tilde signals in terms of the measured PMs from

$$\begin{aligned}\tilde{w}_X(t + \tau_X) &= s_+(t + \tau_X) \\ &= F_{+X0} s_+(t) + F_{\times X0} s_\times(t);\end{aligned}\quad (26)$$

where the notation for F_{+X0} and $F_{\times X0}$ was presented in section 2 and here s_+ and s_\times denote the measured PMs. Then, we can subtract this reconstructed signal from the original strains to check whether the spin-2 polarization modes account for the observed GW. An appropriate tool to study this situation is the optimized measure Λ introduced in Moreschi (2024); which allows to compare two strains.

In each of the following two graphs, we compare the strains $-H$ and L on the two observatories, Hanford and Livingston after applying a bandpass filter of $[30,350]$ Hz. In Fig. 39 we present the graph of the measure Λ for the filtered strains and for the strain after the subtraction of the reconstructed signals from the spin-2 polarization modes.

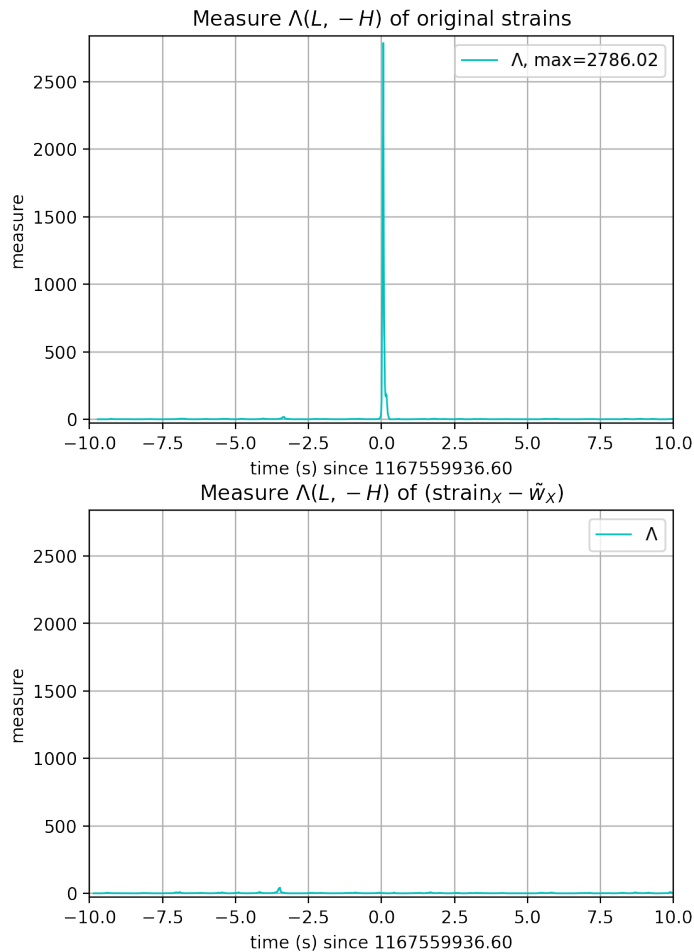


Fig. 39 On the top graph, the values of the measure Λ close to the reference event time for the original filtered strains of GW170104, and on the bottom for the strains after the subtraction of the reconstructed signals from the spin-2 polarization modes. The residual is undetected.

If the original GW had a significant contribution from spin-1 and/or spin-0 polarization modes then there should appear some residual in the bottom graph of Fig. 39. The fact that the measure Λ behaves as ambient noise close to the reference event time, after the subtraction of the reconstructed signals from the spin-2 polarization modes, indicates that the GW signals for GW170104 can be completely understood in terms of the spin-2 polarization modes. That is, no other polarization modes of spin-1 or spin-0 contribute to this detected GW signal.

For this reason we claim that there is no need for more observatories to make a measurement of the polarization modes of this gravitational wave.

10 Nominal time shift for GW150914

To determine a nominal time shift for strain H with respect to strain L for the GW150914 event, we used the original filtered strains and applied additional bandpass filtering, testing several window widths for each analysis. We initially studied the strain in the frequency band $[22,1024]$ Hz, where a natural signal duration of 0.5s appears due to low-frequency contributions at early times. However, the study of the Λ measure (Moreschi, 2024) proved to be excessively noisy. Therefore, we tested several frequency ranges and ultimately chose to work in the $[27,500]$ Hz band. This choice suggests an optimal window length of 0.15s for the relevant signal. Applying the window width $wl = 0.15$ s yields the behavior for the Λ measure shown in Fig. 40.

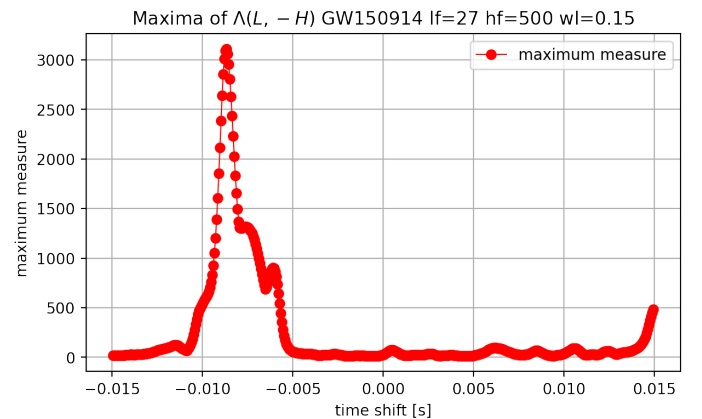


Fig. 40 This graph shows the behavior of mathematical evaluation Λ of the OM measure as a function of shift of the Hanford data with respect to the Livingston data for a window of 0.15s and a band limiting frequency filter of $[27,500]$ Hz.

When we apply this analysis to a window width of $wl = 0.075$ s, the Λ measure exhibits the behavior shown in Fig. 41.

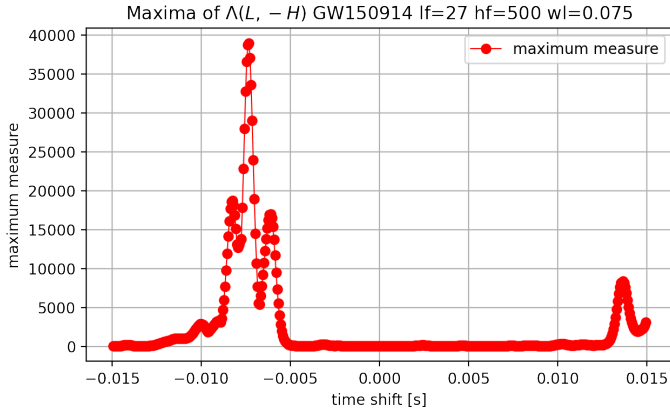


Fig. 41 This graph shows the behavior of mathematical evaluation Λ of the OM measure as a function of shift of the Hanford data with respect to the Livingston data for a window of 0.075s and a band limiting frequency filter of [27,500]Hz.

The fact that these two window widths yield different results suggests that the two observatories may have recorded different components of the spin-2 polarization modes of the gravitational wave. Using this preliminary information, we estimate the time shift for H as the weighted average of these two values, based on the relationship between the highest frequency in the short window strain and the dominant frequency contribution in the wide window strain, obtaining $sh_H = -0.007568s$.

To examine the relationship between both strains during the relevant time interval near the event time, Fig. 42 shows both the -H and L strains when H is shifted by sh_H .

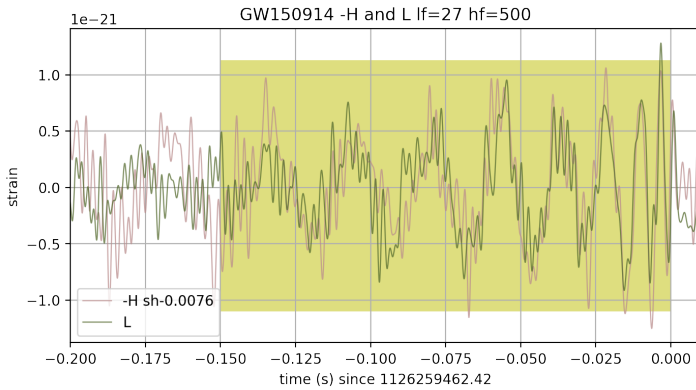


Fig. 42 Strains of -H and L with a band limiting frequency filter of [27,500]Hz and with $sh_H = -0.007568s$. The colored rectangular region indicates the initial width of the window used in the measure.

An impressive coincidence in both form and phase can be observed between the two signals in the colored region, which has the width of the initial window length wl .

It should be noted that in the original presentation of GW150914 (Abbott et al, 2016a), a nominal time shift of -0.0069s was reported for strain H with respect to L, which

represents a difference of $6.7 \times 10^{-4}s$ between the two estimates. While this may appear to be a small separation, and indeed is small with regard to source localization, it is significant for polarization mode decomposition. For this reason, we strive to be as precise as possible with this estimate.

11 Study of GW150914 in the time-frequency domain

Figures 43 and 44 show the signals in the time-frequency domain through their corresponding scalograms.

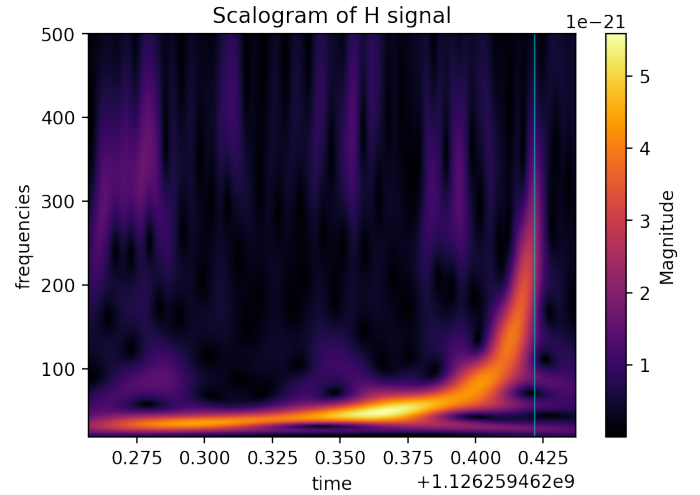


Fig. 43 Detail of the strain of LIGO detector H for GW150914 with a pass band of [27,500]Hz.

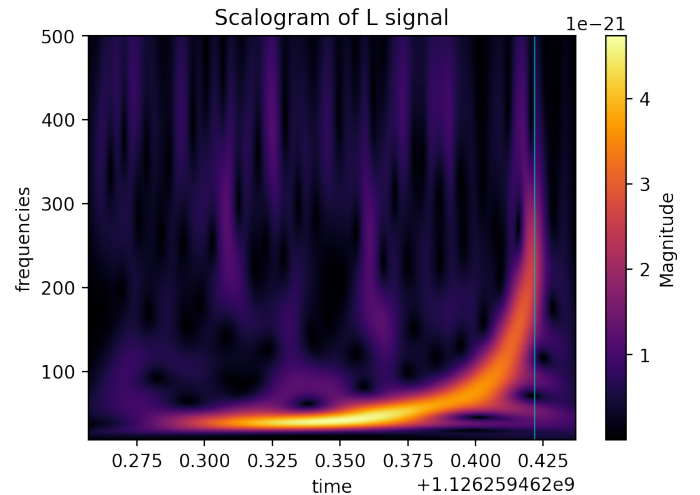


Fig. 44 Detail of the strain of LIGO detector L for GW150914 with a pass band of [27,500]Hz.

These two graphs show clear chirp-like signals observed by both observatories.

12 Localization of GW150914

Applying the L2D+PMR procedure to this event, we calculate its localization and present the final 0.9 confidence level region for GW150914 in Fig. 45.

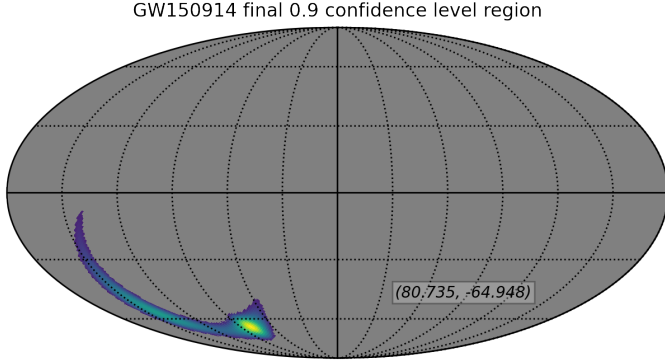


Fig. 45 Final sky localization for the source of the GW150914 event, with 0.9 confidence level region of measure M_u . The two numbers between parentheses denote the preferred central position as longitude and latitude.

This result should be compared with the 90% credible localization region obtained using the LIGO LALInference method.

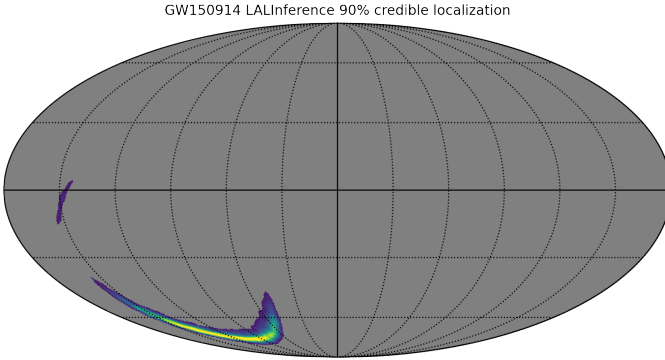


Fig. 46 Sky localization from LIGO team with LALInference method.

Both regions, shown in Figs. 45 and 46, are very similar in location and extent.

13 Reconstruction of the spin-2 polarization modes of GW150914

The reconstructed polarization modes of GW150914 are presented in Fig. 47.

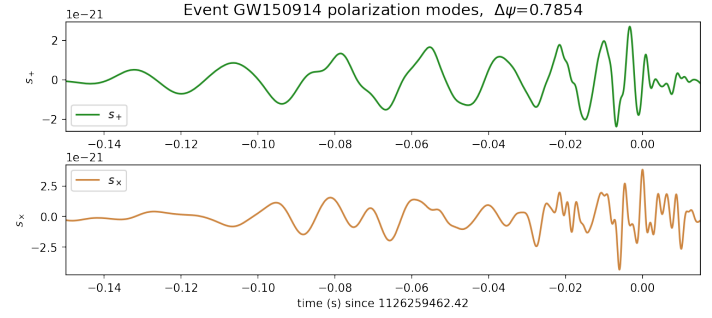


Fig. 47 Polarization modes $+$ and \times close to the reference time of the GW150914 event.

Figure 47 shows that while s_+ exhibits a familiar chirp-like shape, s_\times does not display a strong signal and appears to contain more noise. This observation is corroborated in Fig. 48, which includes the error bands.

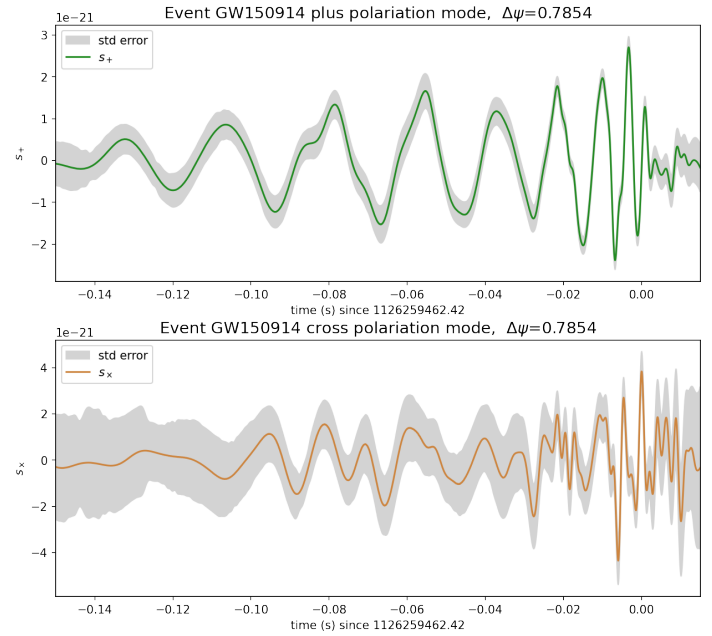


Fig. 48 Polarization modes of the event GW150914 with estimated error bands, in the region close to the nominal event time.

Figure 48 confirms that the estimated error for s_\times is considerably larger than the error for s_+ . This is consistent with the fact that both observatories recorded nearly identical polarization mode components of the gravitational wave. This can also be verified by comparing the denoised -H and L signals, as shown in Fig. 49.

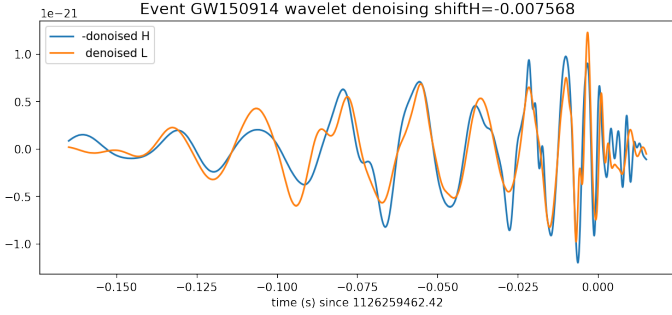


Fig. 49 Denoised signals of the GW150914 event.

Figure 49 demonstrates the remarkable similarity between both denoised signals, and the similarity with the s_+ component shown in Fig. 47 is also notable.

Due to space constraints, we do not include the spin-2 polarization modes of GW150914 in multiple frames here, but present only the $+$ and \times components in a frame that accentuates the diminishing of one component, as shown in Fig. 50.

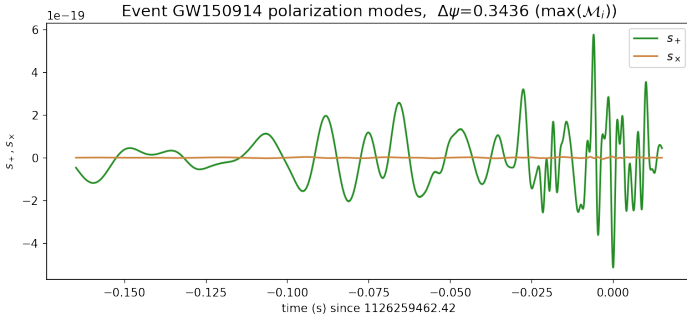


Fig. 50 Polarization modes of GW150914 in selected frame in which one of the components has negligible values.

Figure 50 shows that the \times component is negligible compared to the $+$ component; however, the \times component exhibits significant noise, as demonstrated in Fig. 51.

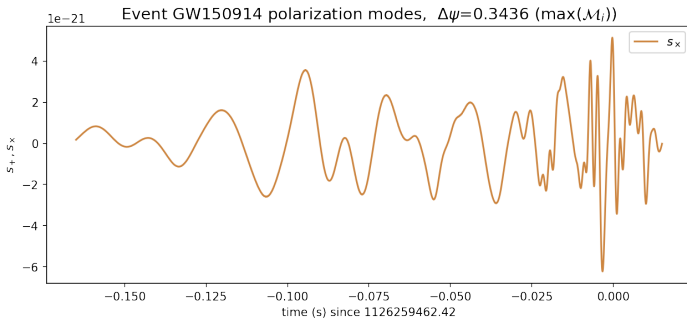


Fig. 51 The \times polarization modes of GW150914 in selected frame.

It must be emphasized that to achieve the impressive cancellation shown in Fig. 50, the polarization mode reconstruction must be performed at the location of the maximum of \mathcal{M}_i , near the nominal delay ring, as shown in Fig. 53. All this indicates that in this case as well, both LIGO observatories detected nearly identical spin-2 components of the gravitational wave. Since these reconstructions were performed using the algebraic and geometrical properties inherent to the spin-2 nature of gravitational waves, the preceding graphs provide direct evidence of the spin-2 nature of the detected signals.

The remarkable cancellation of s_\times shown in Fig. 50 warrants further discussion. Using strains recorded at two different gravitational wave observatories, each with intrinsic independent noise, we applied filtering techniques and subjected the data to algebraic manipulation consistent with our source localization procedure. We then reconstructed the polarization modes and found that one component is essentially zero compared to the other in a particular polarization frame. Since this flat response, shown in Fig. 50, cannot be generated by chance, the inevitable conclusion, before any discussion of the content and meaning of this extraordinary cancellation, is that we could not have achieved this result if our source localization procedure and spin-2 polarization mode reconstruction technique were incorrect. Therefore, we interpret this impressive cancellation as strong evidence for the consistency of the L2D+PMR procedure.

14 Final comments

In order to gain confidence that a perturbation in a GW detector has an astrophysical origin one normally requires to record some signal in at least two detectors. However, how can one be sure that these would correspond to a GW rather than just a mere coincidence, even if such a coincidence is highly unlikely? The answer lies in testing whether the signals behave as GWs; which is done by representing them in terms of its polarization modes. In this article, we have completed this program for the GW170104 and GW150914 events. We have successfully established the reconstruction of the polarization modes of detected GWs, in a model independent approach, using the data recorded from only the two LIGO observatories. This is a fundamental result in the observational study of gravitational waves.

At this point it is important to mention that it is widely belief that in order to perform a measurement of the polarization modes of a GW one needs about five detectors; so that one is able to separate the contributions from the different possible polarization modes. However, we remark in appendix A that for a GW of astrophysical origin, modeled by an asymptotically flat spacetime, the only possible detectable polarization modes are those with spin 2.

Independently of the previous theoretical considerations, our findings represent the first explicit reconstruction of the spin-2 polarization modes of GWs in terms of time series.

It is natural to ask what are we doing differently to obtain localization results from data of just two observatories. And the answer is manifold that we summarize in: that we are optimizing the use of spin-2 polarization geometrical equations, that we are using a new denoising technique and that we are employing a convenient measure on the celestial sphere.

The reliability of our procedure can be inferred from several results. One of them is the fact that the reconstructed polarization modes account for all the content of the detected signal, as is shown explicitly in the bottom graph of Fig. 39; which shows the consistency of our method with the spin-2 nature of the detected signal. But to consider more validation arguments for our procedure, we also have included 10 simulations where we have calculated the localization from the injection of simple synthetic signals at different locations and with a nontrivial initial eccentricity. We have also reconstructed satisfactorily the polarization modes of the original injected signal. Since the procedure depends only (Abbott et al, 2018) on the geometry of a gravitational wave's strain and its direction of propagation, not on the details of any specific theory of gravity, we have built a very simple signal out of the spin-2 polarization modes, that is described in appendix L. We have chosen the position of ten synthetic sources at different sky locations corresponding to a single different delay time. In section 6 we present several graphs showing the reasonable accuracy and precision properties of our localization methods. In Figs. 31 and 32 we show the reconstructed spin-2 polarization modes of the synthetic signals; where one can check the excellent similarity with the original polarization modes, used to construct the signals. All these demonstrate the coherence and reliability of our method.

After the L2D+PMR procedure is applied one is in position to undertake a research on trying to model the detected GW and polarization modes in terms of specific parameters. In this article we have not attempted to get into the detail astrophysical interpretation of our results; instead we have concentrated in the presentation of a new procedure that allows for the localization of a GW source using data from just two detectors, and that also permits the reconstruction of the PMs from this data.

Let us note that our preliminary and final localization for GW170104 are concentrated in regions of the celestial sphere that are close to those predicted by Bayestar and LALInference of LIGO, that we reproduce in Figs. 35 and 36.

The results presented above confirm the expectation that a GW of astrophysical origin should be completely represented in terms of spin-2 polarization modes; since we have measured no contributions from spin 1 and spin 0 polarization modes to GW170104. This not only authenticates the recorded signals to be actual GWs, but also validates our understanding on the nature of them.

The GW150914 event presents a case of a very strong GW signal accompanied by high-amplitude noise, which is

characteristic of the first observing run. We have demonstrated in Section 10 the subtleties involved in determining a nominal time shift for strain H with respect to L. The relationship between the preliminary and final time shifts shown in the graphs is consistent with the effective single-site timing accuracy for each detector (Abbott et al, 2020; Bartos et al, 2010), on the order of 10^{-4} s, which we have neglected in our treatment, and with the phase uncertainty (Abbott et al, 2017a) reported by the LIGO team.

Regarding intersite timing accuracy, it was claimed (Abbott et al, 2020) that the absolute timing discrepancy from UTC, and therefore between detectors, was no larger than 10μ s. The LIGO team concluded that the total uncertainty in the signal was less than 10% in magnitude and 10° in phase from 20Hz to 1kHz during the GW150914 observation. This is related to the fact that GW150914 was detected during the engineering run ER8 (Abbott et al, 2020), which immediately preceded the formal start of the first run O1. Naturally, one expected that at these early stages there would be ongoing efforts to control systematic errors and unwanted uncertainties.

For these reasons, our strategy was to develop our procedure using data from later observing runs. The effects of different uncertainties in strain calibrations on each step of our procedure will be the subject of further study. In this article, we present our results assuming no systematic errors in strain calibration. The impressive anticorrelation of signals in both observatories can already be observed by comparing the strains shown in Fig. 42.

The fact that our 0.9 confidence level region for GW150914 nearly overlaps with the 90% credible localization calculated using the LALInference method indicates agreement between both approaches for GW source localization in this case.

The graph corresponding to GW170104 polarization modes in Fig. 37 suggests that both LIGO observatories recorded nearly identical PM components of the GW. This observation is corroborated by the PM graphs presented in other polarization frames (Figs. 55-59), where the components become very similar in some frames while one component becomes negligible in others. We observed the same phenomenon with GW150914, as shown in Fig. 47. While the + component exhibits a clean, expected waveform, the \times component appears to be dominated by noise, a conclusion supported by the corresponding error graphs in Fig. 48. The clearest indication of this behavior comes from the noticeable cancellation of one polarization mode in a selected polarization frame (Fig. 50) and through direct comparison of the denoised signals shown in Fig. 49. The physical information contained in the spin-2 polarization modes presented here will be analyzed in dedicated future studies.

It is curious that both GW events analyzed here exhibit the same characteristic: each observatory detected nearly identical spin-2 PM components of the respective GW (with one being approximately the negative of the other). The

degree of this effect is particularly striking in Fig. 50, where one polarization mode component appears to be few orders of magnitude smaller than the other.

As discussed in Section 8, the polarization mode reconstruction algebra from two-observatory strain data has a remarkable property: for highly (anti)correlated signals, the calculation involves subtracting the Hanford and Livingston measurements, thereby increasing noise susceptibility. This explains why the reconstructed polarization modes for GW170104 appear noise-dominated, while the + polarization mode component of GW150914 shows physically meaningful structure. The difference stems from the signal-to-noise ratio in each case, the cWB Search Pipeline reports a Network SNR of 13.0 for GW170104 compared to 25.2 for GW150914. The higher SNR of GW150914 provides sufficient signal strength to enable meaningful polarization mode reconstruction. This represents the first direct measurement of a spin-2 polarization mode of a gravitational wave.

These observations encourage further investigation into applying these novel methods to real gravitational wave events. The significance of the results presented here suggests that such studies will yield valuable scientific insights.

Gravitational wave observatories undergo continuous improvements, with each scientific run achieving lower intrinsic noise levels and enhanced sensitivity to weaker signals. This increased sensitivity expands the observable volume range, enabling the detection of more events with favorable signal-to-noise ratios. We are therefore eager to access strain data from the fourth observing run, which is expected to provide detailed gravitational wave observations from multiple observatories. This presentation suggests that our procedure will prove valuable for analyzing these future detections.

In Appendices we have included details of GW analysis that deserve an extended explanation but that would enlarge unnecessary the main part of the text.

In future work we intend to apply these techniques to other GW events, expand on the details of our methods, and continue to improve and refine them.

Acknowledgments

This work is possible thanks to the open data policy of the LIGO Scientific Collaboration, the Virgo Collaboration and Kagra Collaboration; who are giving freely access to data through the Gravitational Wave Open Science Center at <https://gwosc.org>; which is described in Abbott et al (2021) and Abbott et al (2023).

We have used python tools included in the project PyWavelets(Lee et al, 2019).

We acknowledge support from SeCyT-UNC and CONICET.

The inclusion of the GW150914 event in this article is due to the interaction with an anonymous referee to whom we are grateful; since the discussion of these two events becomes essential to grasp the nature of our procedure.

We are very grateful to Ezequiel F. Boero for comments and proof reading and Emanuel Gallo for numerous deep discussions and indicating several improvements. We also thank Maximiliano Isi for fruitful elaborated discussions.

Declarations

Data Availability:

The time series of the calculated spin-2 polarization modes for event GW170104 and GW150914 can be requested via email to the author. We intend to publish this and other PMs on the web in the future. The numerical calculation is described in the article.

Ethics declaration:

not applicable.

APPENDICES

A Basic theoretical framework

Up to now the most successful description of gravitational phenomena comes from the equivalence principle(Einstein, 1911); which has been tested to high precision(Touboul et al, 2022). An important implication of this principle, is that the gravitational effects are encoded in the curvature of the spacetime metric.

In particular, present “L” shape gravitational-wave detectors intend to measure the characteristics of a passing GW by observing the effects on mirrors at the ends of the arms. The relative motion of each pair of mirrors is described by the geodesic deviation equation, that for the deviation vector ξ^a can be expressed as(Wald, 1984)

$$a^a = t^c \nabla_c v^a = t^c \nabla_c (t^b \nabla_b \xi^a) = R_{cbd}{}^a \xi^b t^c t^d; \quad (27)$$

where t^b is a unit timelike vector orthogonal to ξ^a and a^a is the acceleration. For describing the components of the curvature tensor $R_{cbd}{}^a$ we use the conventions of Pirani (1965), which agrees with Penrose and Rindler (1984). It is also advantageous to use a null tetrad to describe the components of the curvature and therefore, the nature of the waves, since they travel along null directions. One common nomenclature for a null tetrad, adapted to these type of situations is to use a real null vector (ℓ^a) to point in the direction of the propagation; two complex (spacelike) null vectors (m^a, \bar{m}^a) are chosen perpendicular to the propagation direction, and a fourth real null vector (n^a) is chosen perpendicular to the last two and with unit contraction with the first ($g_{ab} \ell^a n^b = 1$). This is the basis for the Geroch-Held-Penrose(GHP) formalism(Geroch et al, 1973) which is useful for the geometric discussion of a variety of situations in which this type of basis appears naturally. When contracting this basis with different objects one obtains quantities with spin weight.

The local null tetrad can be related to a Cartesian frame by: $\ell^a = \frac{1}{\sqrt{2}}(t^a + e_3^a)$, $n^a = \frac{1}{\sqrt{2}}(t^a - e_3^a)$, $m^a = \frac{1}{\sqrt{2}}(e_1^a + ie_2^a)$

and $\bar{m}^a = \frac{1}{\sqrt{2}}(e_1^a - ie_2^a)$; where the e_j form the unit spacelike basis, and $i^2 = -1$, is the complex basis number.

Then, one can express the polarization modes in terms of following curvature components:

$$R_+ = R_{0101} - R_{0202} = R_{0m0m} + R_{0\bar{m}0\bar{m}} = \Re e\{\Psi_0 - 2\Phi_{02} + \bar{\Psi}_4\}, \quad (28)$$

$$R_\times = R_{0102} + R_{0201} = -i(R_{0m0m} - R_{0\bar{m}0\bar{m}}) = \Im m\{\Psi_0 - 2\Phi_{02} + \bar{\Psi}_4\}, \quad (29)$$

$$R_R = R_{0101} + R_{0202} = 2R_{0m0m} = \Phi_{00} - 2(\Re e\{\Psi_2\} + 2\Lambda) + \Phi_{22}, \quad (30)$$

$$R_{vx} = R_{0103} + R_{0301} = 2R_{0103} = \Re e\{-3(\Psi_1 + \Phi_{01}) + (\bar{\Psi}_3 + \Phi_{12})\}, \quad (31)$$

$$R_{vy} = R_{0203} + R_{0302} = 2R_{0203} = \Im m\{-3(\Psi_1 + \Phi_{01}) + (\bar{\Psi}_3 + \Phi_{12})\}, \quad (32)$$

$$R_M = R_{0303} = \Psi_2 + \bar{\Psi}_2 + 2\Phi_{11} - 2\Lambda = 2(\Re e\{\Psi_2\} + \Phi_{11} - \Lambda). \quad (33)$$

It is worthwhile noting that R_+ and R_\times are the real and imaginary parts of a spin 2 quantity (Geroch et al, 1973), and R_{vx} and R_{vy} are the real and imaginary parts of a spin 1 quantity, while R_R and R_M are spin 0 quantities.

These six polarization modes were studied in Eardley et al (1973a) and Eardley et al (1973b) for the specific case of plane waves. In Eardley et al (1973a) they stated: ‘‘General relativity permits only the two Ψ_4 modes.’’; which sometimes has been taken as a general absolute truth. However, the mathematics of a Universe filled with a plane wave is very different from the description of an isolated system, that is usually employed for the description of a bound system, as for example a binary black hole system.

An expected quality of a relativistic theory of gravity is to be able to provide good representations of isolated system, so that the contribution to the curvature from these isolated systems approaches zero as one moves away from the central region of the system. This is expected even in a cosmological contexts when one considers compact bounded systems faraway from other bodies. That is, the full Riemann tensor can be understood as $R_{abc}{}^d = R_{abc}{}^d{}^{(B)} + R_{abc}{}^d{}^{(GW)}$ where (B) refers to a slow varying background and (GW) stands for the rapidly varying contribution due to a passing GW (See section 1.5 of reference Jaranowski and Krolak (2009)). The fact is that the gravitational-wave observatories are designed to be sensitive to the (GW) contribution to the curvature; for this reason in gravitational-wave studies one normally does not distinguish between $R_{abc}{}^d$ and $R_{abc}{}^d{}^{(GW)}$.

In an scenario in which there are no *a priori* cosmological assumptions, the idea of the notion of an isolated system independent of a particular field equation led to the concept of general asymptotically flat spacetimes (Moreschi, 1987). In this reference it was studied the general case of a spacetime which is asymptotically flat at future null infinity (\mathcal{I}^+) with the basic behavior

$$R_{abc}{}^d = f(\Omega)\hat{R}_{abc}{}^d + \delta R_{abc}{}^d, \quad (34)$$

where Ω is the conformal factor used to define future null infinity, $f(\Omega)$ is a monotonic function with the property $\lim_{\Omega \rightarrow 0} f = 0$, $\hat{R}_{abc}{}^d$ is a regular tensor at \mathcal{I}^+ and $\delta R_{abc}{}^d$ is a tensor in a neighborhood of \mathcal{I}^+ that goes to zero faster than $f(\Omega)$ for $\Omega \rightarrow 0$; for details see Moreschi (1987). One of the remarkable findings in this work was that independently of the functional form of $f(\Omega)$, one can establish the

asymptotic behavior of the radiation field, namely

$$\Psi_4 = -\Omega \ddot{\sigma}_0 + O(-1), \quad (35)$$

$$\Psi_3 = -\Omega^2 \ddot{\delta}_0 \dot{\sigma}_0 + O(-2), \quad (36)$$

and

$$\Phi_{22} = O(-1); \quad (37)$$

where σ_0 encodes the asymptotic shear of the bundle defined by the vector field ℓ , dots mean time derivatives, a quantity $h(\Omega)$ is said to be $O(q)$ if $\lim_{\Omega \rightarrow 0} \Omega^q h = 0$, and $\ddot{\delta}_0$ is the edth operator (Geroch et al, 1973) of the unit sphere. This is a very strong result, that it says that independently of the field equation, if the GW is due to the gravitational radiation of an astrophysical isolated system, then the possible observable is just Ψ_4 ; since all the other component fields decay too fast with distance. In any case, for the sake of completeness we describe next the asymptotic leading order behavior of the R_{0X0Y} components for the case of a general asymptotically flat spacetime but with $f(\Omega) = \Omega = \frac{1}{r}$, where r is an affine distance:

$$R_{0m0m} = \frac{1}{2} \frac{\bar{\Psi}_4^0}{r} + O(-1), \quad (38)$$

$$R_{0m0\bar{m}} = \frac{1}{2} \frac{\Phi_{22}^0}{r^2} + O(-2), \quad (39)$$

$$R_{0m03} = \frac{1}{2\sqrt{2}} \frac{\bar{\Psi}_3^0}{r^2} + O(-2), \quad (40)$$

$$R_{0303} = 2 \frac{\Re e\{\Psi_2^0\}}{r^3} + O(-3); \quad (41)$$

where each quantity with a supra index 0 represents the leading order behavior. In terms of the polarization modes defined above one has:

$$R_+ = \frac{\Re e\{\bar{\Psi}_4^0\}}{r} + O(-1), \quad (42)$$

$$R_\times = \frac{\Im m\{\bar{\Psi}_4^0\}}{r} + O(-1), \quad (43)$$

$$R_R = \frac{\Phi_{22}^0}{r^2} + O(-2), \quad (44)$$

$$R_{vx} = \frac{\Re e\{\bar{\Psi}_3^0\}}{r^2} + O(-2), \quad (45)$$

$$R_{vy} = \frac{\Im m\{\bar{\Psi}_3^0\}}{r^2} + O(-2), \quad (46)$$

and

$$R_M = 2 \frac{\Re e\{\Psi_2^0\}}{r^3} + O(-3). \quad (47)$$

The above discussion indicates that it is natural to describe the polarization state in terms of components which behave as quantities of spin weight 2, 1 or 0; making reference in the case of spin weight 0 of the two channels, that we call the mass channel, associated to $\Re e\{\Psi_2^0\}$, and

the matter radiation channel, associated to Φ_{22}^0 . The assignment of the name ‘mass channel’ to the component $\Re\{\Psi_2^0\}$ is due to the fact that it contributes to the calculation of total momentum (Moreschi, 2004) at future null infinity.

It is deduced then that although the equations for the polarization modes are algebraically compatible with those used in the weak plane wave models of reference Eardley et al (1973a), our equations 38-41, or 42-47, show that only the spin 2 modes are the astrophysical observable polarizations; in other words, if the other modes or channels were detected, then they would not have an astrophysical distant origin. It is probably worthwhile to emphasize that we have not assumed a particular field equation, but only that isolated systems are well represented by general asymptotically flat spacetimes (Moreschi, 1987).

In summary, within this set of gravitational theories, in a typical astrophysical scenario one expects to record only spin 2 polarization gravitational-wave signals. For this reason, in this article we concentrate only in the presence of these two components of the polarization of the gravitational wave.

B Basis and coordinate systems

Based on the results from previous efforts found in the literature, we expect to have errors in the localization of the sources of the order of one degree in angular coordinates. This allows us to consider the local geometry, used in the astrophysics determinations, to be given by a flat geometry; in agreement with the discussions of (Ashby, 2003).

The position and orientation of the observatories are defined in terms of geocentric coordinates that rotate with the Earth. More specifically one normally uses the International Terrestrial Reference System (ITRS). We also need to use the Earth Rotation Angle (ERA) which is the angle between the Terrestrial Intermediate Origin and the Celestial Intermediate Origin, positively in the retrograde direction. Its specification is determined by the International Earth Rotation and Reference Systems Service (IERS) (Petit et al, 2010) conventions.

C Basis for the calculation of the detector pattern functions

Our conventions agree with those of Poisson and Will (2014) with a slight change in the notation.

Let $\{\hat{e}_1, \hat{e}_2, \hat{e}_3\}$ be the orthonormal basis for a detector. One can perform first a rotation around \hat{e}_3 of an angle ϕ , so that one obtains:

$$\hat{e}_1'' = \cos(\phi)\hat{e}_1 + \sin(\phi)\hat{e}_2 \quad (48)$$

$$\hat{e}_2'' = -\sin(\phi)\hat{e}_1 + \cos(\phi)\hat{e}_2 \quad (49)$$

$$\hat{e}_3'' = \hat{e}_3; \quad (50)$$

then one performs a rotation θ around the new direction \hat{e}_2'' ; so that one obtains:

$$\begin{aligned} \hat{e}_1' &= \cos(\theta)\hat{e}_1'' - \sin(\theta)\hat{e}_3'' = \cos(\theta)\cos(\phi)\hat{e}_1 \\ &\quad + \cos(\theta)\sin(\phi)\hat{e}_2 - \sin(\theta)\hat{e}_3 \end{aligned} \quad (51)$$

$$\hat{e}_2' = \hat{e}_2'' = -\sin(\phi)\hat{e}_1 + \cos(\phi)\hat{e}_2 \quad (52)$$

$$\begin{aligned} \hat{e}_3' &= \sin(\theta)\hat{e}_1'' + \cos(\theta)\hat{e}_3'' = \sin(\theta)\cos(\phi)\hat{e}_1 \\ &\quad + \sin(\theta)\sin(\phi)\hat{e}_2 + \cos(\theta)\hat{e}_3. \end{aligned} \quad (53)$$

The final degree of freedom is to perform a rotation ψ around the new axis \hat{e}_3' , and we also carry out an inversion of the second and third basis vectors, so that one obtains:

$$\tilde{e}_1 = \cos(\psi)\hat{e}_1' + \sin(\psi)\hat{e}_2' \quad (54)$$

$$\tilde{e}_2 = \sin(\psi)\hat{e}_1' - \cos(\psi)\hat{e}_2' \quad (55)$$

$$\tilde{e}_3 = -\hat{e}_3'; \quad (56)$$

which agrees with ref. Poisson and Will (2014), by noting for example that our \tilde{e}_1 is theirs \mathbf{e}_X . In this way, \tilde{e}_3 points in the direction of the propagation of the GW.

D Reference frames for the propagation of the gravitational wave

Normally the basis for the GW is defined with respect to a unit vector $\hat{k} = \tilde{e}_3$ in the direction of the propagation and two other orthonormal vectors defining an oriented basis.

In our work we think of a GW as coming from the direction (δ, α) in the sky, which could be identified with standard equatorial coordinates (Bradt, 2004), but instead to use the astronomical definitions, we will use the standard geometrical angles, so that we use radians with the ranges: $\delta \in [0, \pi]$ (-declination using colatitude) and $\alpha \in [0, 2\pi]$ (right ascension in radians) also eastward; and with origin at the vernal equinox.

Then, we can define the vector \hat{k} by

$$\hat{k} = -(\sin(\delta)\cos(\alpha), \sin(\delta)\sin(\alpha), \cos(\delta)), \quad (57)$$

and

$$\hat{\delta} = (\cos(\delta)\cos(\alpha), \cos(\delta)\sin(\alpha), -\sin(\delta)), \quad (58)$$

$$\hat{\alpha} = (-\sin(\alpha), \cos(\alpha), 0); \quad (59)$$

with orientation $\{\hat{\alpha}, \hat{\delta}, \hat{k}\}$, noting that in a Mollweide projection, $\hat{\alpha}$ points to the eastward direction (left) and $\hat{\delta}$ points to the south (down). In this way, \hat{k} points to us from the celestial coordinates (δ, α) .

The + and \times polarization components are defined with respect to this $\{\hat{\alpha}, \hat{\delta}\}$ basis.

E Detector pattern functions for GW

Let us start by noting that in the literature, different authors use diverse language to refer to the polarization properties of a GW. So here we first review our approach to the subject and then relate to other point of views found in publications.

The perturbations produced by a GW are thought as local variations of the curvature tensor, which when expressed in terms of a local basis can be described by field components as the ones used in Eardley et al (1973a), namely the Weyl components Ψ_4 , Ψ_3 and Ψ_2 , and the Ricci component Φ_{22} . Since a gravitational-wave detector is supposed to have a linear response to these perturbations, one can make the following decomposition of the signal $s(t)$ recorded by an observatory:

$$s(t) = \sum_p F_p(\theta, \phi, \psi, t) s_p(t); \quad (60)$$

where p is used to distinguish among the different types of polarizations.

Very often in the literature one finds the discussion of polarization states to be based directly in perturbations of the metric (Nishizawa et al, 2009; Poisson and Will, 2014); where one can map the perturbations of the curvature to variations of the metric (Poisson and Will, 2014).

The six pattern functions presented below, correspond to the complete algebraic study of the curvature matrix appearing in the geodesic deviation equation; however, we have presented arguments above that indicate that in a normal astrophysical situation, the $+$ and \times modes would be the more relevant ones. In reconstructing the polarizations s_+ and s_\times for each event, one has

$$s_X(t + \tau_X) = F_{+X}(\theta_X, \phi_X, \psi_X, t) s_+(t) + F_{\times X}(\theta_X, \phi_X, \psi_X, t) s_\times(t). \quad (61)$$

Note that our choice for the angular terrestrial basis agrees with the choice of reference Poisson and Will (2014); which means that our signs in the calculations of the *detector pattern functions* should agree with this reference. More specifically, using prime for the quantities of reference Poisson and Will (2014); we have that the complete set of pattern functions are

$$F_+ = F'_+ = \frac{1}{2}(1 + \cos(\theta)^2) \cos(2\phi) \cos(2\psi) - \cos(\theta) \sin(2\phi) \sin(2\psi) \quad (62)$$

$$F_\times = F'_\times = \frac{1}{2}(1 + \cos(\theta)^2) \cos(2\phi) \sin(2\psi) + \cos(\theta) \sin(2\phi) \cos(2\psi) \quad (63)$$

$$F_{vx} = F'_{v1} = -\sin(\theta) (\cos(\theta) \cos(2\phi) \cos(\psi) - \sin(2\phi) \sin(\psi)) \quad (64)$$

$$F_{vy} = F'_{v2} = -\sin(\theta) (\cos(\theta) \cos(2\phi) \sin(\psi) + \sin(2\phi) \cos(\psi)) \quad (65)$$

$$F_M = F'_L = \frac{1}{2} \sin(\theta)^2 \cos(2\phi) \quad (66)$$

$$F_R = F'_S = -\frac{1}{2} \sin(\theta)^2 \cos(2\phi); \quad (67)$$

where beyond the spin-2 polarization $+$ and \times we denote with F_{vx} and F_{vy} the spin-1 polarizations and for the spin-0 polarizations we use F_M to denote the mass polarization and F_R to denote the matter radiation polarization. We have

just used the notation in terms of plane waves introduced in reference Eardley et al (1973a); but we describe the modes in terms of available curvature components to an observer of an astrophysical system emitting gravitational radiation; that is, we do not assume that the detected GW is a plane wave.

The pattern functions have several properties, for example that: $F_{+,\times}(\pi - \theta, \pi - \phi, \psi) = F_{+,\times}(\theta, \phi, \psi)$. This means that in their manipulations, having a physically selected direction, one should expect phantom repetitions of corresponding maximum or minimum of functions built out of the pattern functions.

The geometrical data for the gravitational-wave observatories can be obtained from the file LALDetectors.h that is available on the web at several places, for example at git.ligo.org/lscsoft/lalsuite/-/blob/master/lal/lib/tools/LALDetectors.h

F Fitting a universal chirp form

The argument of the trigonometric functions in the fitting mechanism, has the form $\Phi(t) = \phi_c(t) + \phi_f$; where $\phi_c(t) = -2\left(\frac{t_f - t}{5t_{ch}}\right)^{p_c 5/8}$ has the non-trivial time dependence, and the constant ϕ_f denotes a global phase. This means that the fitting of the signal at each detector only requires two parameters to relate to the dynamical dependence of $g(t) \cos(\phi_c(t))$ and $g(t) \sin(\phi_c(t))$. Therefore we organize the calculation by first fitting the parameters $[B_{+cX}, B_{\times cX}]$ to the chirp base, just presented, and then infer the values of $[B_{+X}, B_{\times X}]$ for the phase ϕ_f ; which it can be shown to be given by

$$B_{+X} = \cos(\phi_f) B_{+cX} - \sin(\phi_f) B_{\times cX} \quad (68)$$

$$B_{\times X} = \sin(\phi_f) B_{+cX} + \cos(\phi_f) B_{\times cX}. \quad (69)$$

G Localization by fitting a universal chirp form

As explained in section 5 we study the maxima of M_i ; which best estimates are shown in Fig. 52.

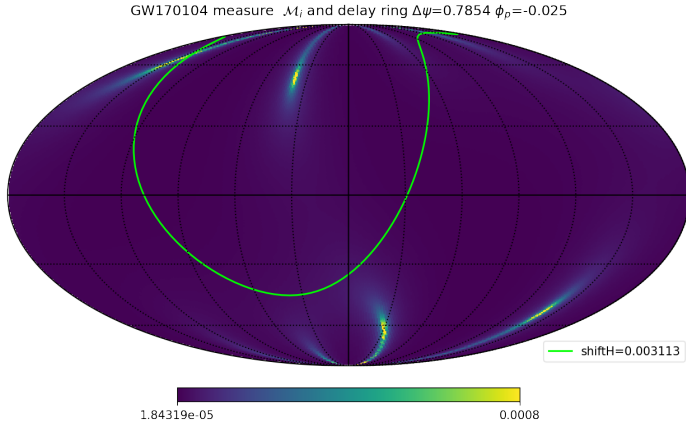


Fig. 52 Plot of the measure \mathcal{M}_i and the delay ring. Sky localization for the source of the GW170104 event shows a signal on the nominal ring on the northern east region.

It can be seen that there are several local maxima, marked in yellow; but only one of them overlap with the delay ring. The other local maxima are considered phantom images due to effects explained in appendix E. The final location is obtained by the product of this signal with the Gaussian of the delay ring; so that it only remains the maximum on the ring, as shown in Fig. 33.

The initial localization for the event GW150914 is shown in Fig. 53.

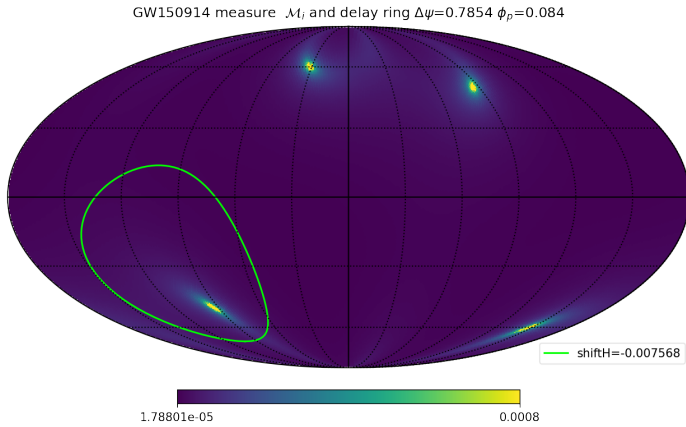


Fig. 53 Plot of the measure \mathcal{M}_i and nominal ring. Sky localization for the source of the GW150914 event is close to the southern part of the ring at (94.16,-49.70) longitude and latitude coordinates.

In the main text it was discussed the impressive anticorrelation of the signals detected at both observatories. This has a strong effect on our procedure which as a consequence it finds the location of the source, close to the nominal delay ring, but separated from it; as it can be seen in the graph of Fig. 53.

H Characteristics of the strain

The event GW170104 is presented in the gwosc.org page as a GWTC-1-confident type, with GPS event time 1167559936.6; corresponding to UTC time: 2017-01-04 10:11:58.6. It was assigned a network SNR of 13.8 and a sky localization area of 1000 square degrees. We have used version v2 of the provided LIGO data.

The one-sigma calibration uncertainties for the strains is informed (Abbott et al, 2017b) to be better than 5% in amplitude and 3° in phase over the frequency range 20-1024Hz.

In Fig. 1 of reference Abbott et al (2017b) they show a signals with a time span of approximately 0.11s, and it has been reported that the Livingston data has been shifted by -0.003s, and the sign of its amplitude has been inverted.

I Determination of the appropriate time delay for the GW170104 event

The initial step in the procedure is to apply the pre-processing filtering techniques to the strains as explained in Moreschi (2019); for which we have used a bandpass of [27,1003]Hz.

In our preliminary study of GW170104 in Moreschi (2024) we have used a window time span of 0.28s, and applying the measure OM we could assign a level of significance $\alpha = 5.5 \times 10^{-8}$ to the detection of similar signals in the two LIGO observatories.

Here we carryout a more detailed analysis on the data of this event. In this study we have used a bandpass in the range [30,350]Hz. The measure OM can be used to study a variety of topics. Its result and sensitivity depends on several parameter, in particular in the time length of the window (wl) that is being used. Although in the preliminary study we used a window of 0.28s; in order to study the behavior of the strains close to the time of maximum amplitude we use also a window of 0.14s as a function of the time shift of the Hanford(H) strain with respect to the Livingston(L) strain. We observe that while for $wl = 0.28s$ the maximum is at $t_{d0} = 0.003235s$; for $wl = 0.14s$ the maximum is at $t_d = 0.003113s$. We will use this last one as the reference time delay between the observatories; since it gives a better representation of the coincidence time for the maximum at high amplitudes.

The corresponding delay ring in the sky is shown in Fig. 54 where we have included also a CMB map from the WMAP team, in order to show the position of the galaxy and so clarify the origin of the equatorial coordinate system.

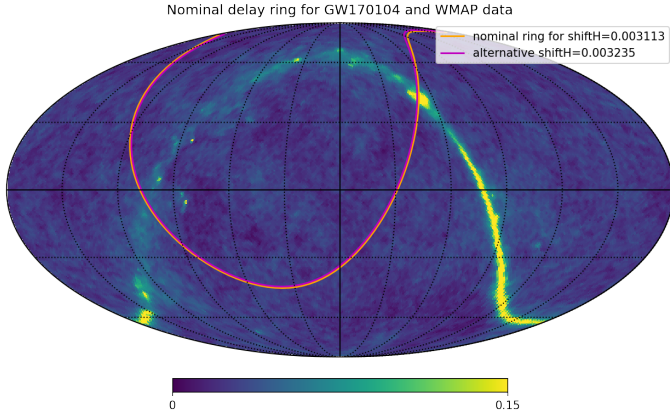


Fig. 54 Nominal delay ring and alternative ring in the sky along with a WMAP graph of the CMB, indicating the position of the galaxy, in order to show the nature of the Mollweide projection in equatorial coordinate system with origin at the center and East towards left.

The determination of the delay ring has an inherent error which we will estimate next. To begin with, the two previous time delays yield two different angles to determine the delay ring. Let us call them Θ_{d0} and Θ_d ; associated with the delay times t_{d0} and t_d respectively. These two delay times already provide us with an operational time delay error $\delta t_{op} = |t_{d0} - t_d| = 0.000122\text{s}$. An estimate of the time delay error can also be calculated from the approximate high frequency contribution at maximum signal. For instance, for this event we have estimated from the scalograms that the maximum relevant contributions close to the chirp time are around $\nu_{max} = 300\text{Hz}$. From this, in the case in which there is no information on the orientation of the observatories and neither there is no information on the location of the source nor on its polarization angle, one could estimate a general time delay error of the order of $\delta t = \frac{T_4}{2} = 0.0004167\text{s}$; where $T_4 = \frac{T}{4} = \frac{1}{4\nu_{max}}$ is a quarter of the period determined by ν_{max} . This in turn induces an error in the determination of the delay ring angle of $\delta\Theta = |\Theta_d - \arccos(\frac{t_d + \delta t}{t_{LH}})|$, where Θ_d is the angle that determines the delay ring and t_{LH} is the time of flight of a signal between the two observatories. We construct a Gaussian distribution around the delay ring considering both contributions to the estimate of the error in the angle that determines the ring and so we take the variance of the ring as $\sigma_r = |\Theta_{d0} - \Theta_d| + \delta\Theta$; which intends to provide a coarse estimate on our error in the determination of the delay ring.

J Other studies of GW170104

Considering other efforts on the localization for GW170104 with electromagnetic counterparts we mention here some of those works. In reference [Goldstein et al \(2017\)](#) they presented the Fermi Gamma-ray Burst Monitor and Large Area Telescope observations of the event GW170104 and claimed that no candidate electromagnetic counterpart was detected by either of the two instruments; although they report upper bounds for the fluxes.

The results from the analysis of hard X-ray and gamma-ray data of the AGILE mission on the localization of GW170104 were reported in [Verrecchia et al \(2017\)](#); and claimed that no transient gamma-ray source was detected over timescales of 2, 20 and 200s starting at the time of the event. However they reported an event E2 occurring at $0.46 \pm 0.05\text{s}$ before the event time which they claim is significant. They could not determine the position of E2, but they obtained the sky region where is the B arc, which is the southern arc reported by the LIGO LALInference method, to which our localization belongs.

In [Savchenko et al \(2017\)](#) the authors reported on the data from the International Gamma-Ray Astrophysics Laboratory; which allowed them to set upper limits on the γ -ray and hard X-ray emission associated with the GW170104 event challenging the possible association of this event with electromagnetic counterparts.

An all-sky high-energy neutrino follow-up search using data from the Antares neutrino telescope has been reported in [Albert et al \(2017\)](#). They found no neutrino candidates within $\pm 500\text{s}$ around the event time nor any time clustering of events over an extended time window of ± 3 months.

In [Stalder et al \(2017\)](#) they reported the peculiar optical transient, ATLAS17aeu; which was discovered 23.1 hr after GW170104 and rapidly faded over the next three nights. They claimed that the observations indicate that ATLAS17aeu is plausibly a normal GRB afterglow at significantly higher redshift than the distance constraint for GW170104 and therefore a chance coincidence.

K Spin-2 polarization modes of GW170104 for different polarization angles

For completeness we also present the polarization modes in the frames with $\Delta\psi = 0$, $\Delta\psi = \frac{\pi}{16}$, $\Delta\psi = \frac{2\pi}{16}$, $\Delta\psi = \frac{3\pi}{16}$ and $\Delta\psi = \frac{\pi}{4}$ close to the nominal event time in Figs. 55-59.

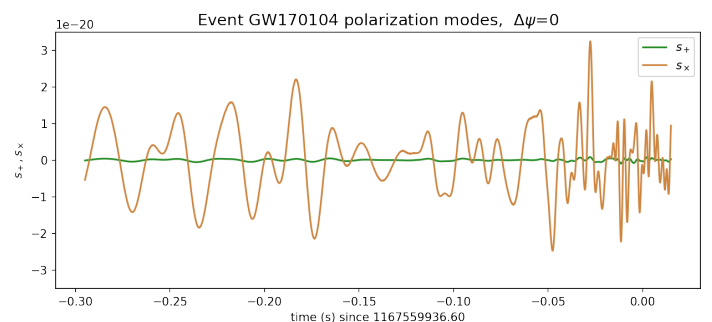


Fig. 55 Polarization modes of GW170104.

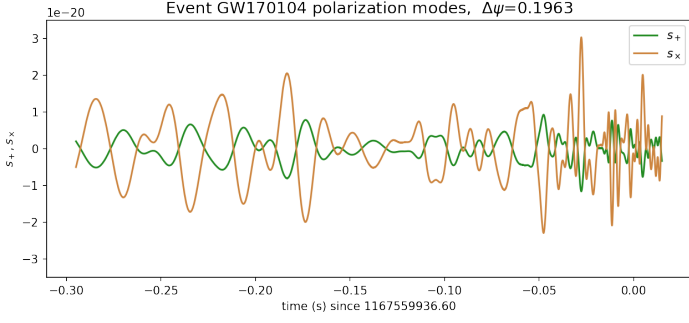


Fig. 56 Polarization modes of GW170104.

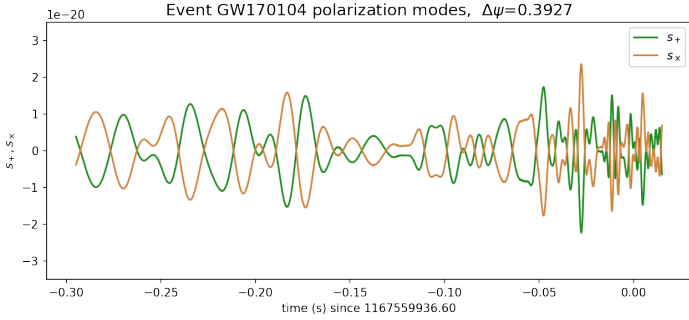


Fig. 57 Polarization modes of GW170104.

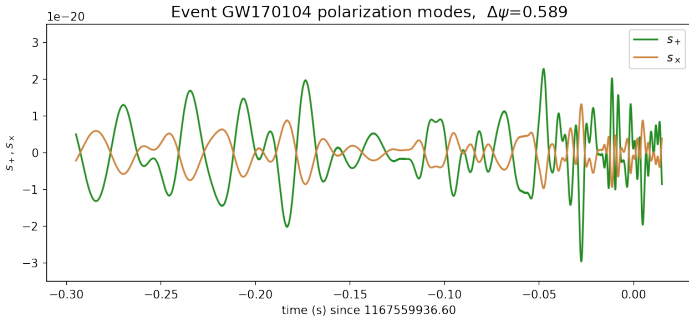


Fig. 58 Polarization modes of GW170104.

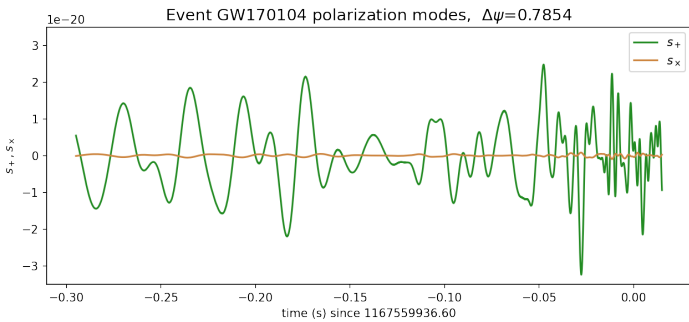


Fig. 59 Polarization modes of GW170104.

It can be seen that for $\Delta\psi = \frac{\pi}{4}$ the polarization modes return to the original values according to the transformation properties of the modes. This indicates that in fact the time series we have calculated with the names s_+ and s_\times behave as spin-2 quantities; within the numerical precision of our calculation.

L Simulation using an injected simple signal

In order to further validate our procedure, we here consider the injection of a simple synthetic signal for a binary black hole coalescence. We use the chirp wave form model (Peters, 1964) described in the textbook on analysis of gravitational-wave data Jaranowski and Krolak (2009) for binary polarization waveforms with radiation reaction effects, with a notation closer to that of Cutler and Flanagan (1994) that we express as:

$$s_+ = \frac{s_0}{a(1-e^2)} \frac{1 + \cos(\iota)^2}{2} \left(-\cos(2\phi(t)) \right) \quad (70)$$

$$+ e \left(-\frac{1}{4} \left(5 \cos(\phi(t) + \phi_0) + \cos(3\phi(t) - \phi_0) \right) \right) \quad (71)$$

$$+ \frac{\sin(\iota)^2}{2(1 + \cos(\iota)^2)} \cos(\phi(t) - \phi_0) \quad (72)$$

$$+ e^2 \left(-\frac{1}{2} \cos(2\phi_0) + \frac{\sin(\iota)^2}{2(1 + \cos(\iota)^2)} \right) \quad (73)$$

$$s_\times = \frac{s_0}{a(1-e^2)} \cos(\iota) \left(-\sin(2\phi(t)) \right) \quad (74)$$

$$- \frac{e}{4} \left(5 \sin(\phi(t) + \phi_0) + \sin(3\phi(t) - \phi_0) \right) \quad (75)$$

$$- \frac{e^2}{2} \sin(2\phi_0) \quad (76)$$

where a is the instantaneous semi-major axis, e the instantaneous eccentricity, ι is the angle between the orbital angular momentum vector of the binary and the line of sight and ϕ_0 the angle of the orbital periaapsis which we assume to occur at $t = 0$. Also $s_0 = \frac{4G^2 M \mu}{c^4 R}$ where for individual masses m_1 and m_2 , $M = m_1 + m_2$ is the total mass and $\mu = \frac{m_1 m_2}{M}$ is the reduced mass. In the case of a circular orbit these expressions reduce to

$$s_+ = -s_0 \frac{1 + \cos(\iota)^2}{2a} \cos \left(-2 \left(\frac{|t_c - t|}{5t_{ch}} \right)^{5/8} + \phi_c \right) \quad (77)$$

$$s_\times = -s_0 \frac{\cos(\iota)}{a} \sin \left(-2 \left(\frac{|t_c - t|}{5t_{ch}} \right)^{5/8} + \phi_c \right), \quad (78)$$

where t_c is the ‘coalescence time’, t_{ch} is the ‘chirp time’, ϕ_c is a reference constant phase, and in this case we use

$$\frac{s_0}{a(t)} = \frac{A_{ch}}{(|t_c - t|^{1/4} + \Delta t_0^{1/4})}, \quad (79)$$

where, we integrate in A_{ch} all the amplitude dependence, and Δt_0 are parameters that are chosen to adjust the amplitude and to limit the divergent pure chirp behavior. We choose the coalescence time to be $t_e - 0.002s$ where t_e is the published reference time for this event.

Let us note that in the literature normally appears the reference to the chirp mass $\mathcal{M} \equiv \mu^{3/5} M^{2/5}$; which is related to the chirp time by $t_{ch} = G\mathcal{M}/c^3$.

For the chirp time we use $t_{ch} = 1.5e-4s$. Also we use $\iota = \frac{\pi}{6}$, $\phi_c = -\pi$ and $\Delta t_0 = 1.e-5s$. Since our method makes use of the data mainly in the inspiral phase and we are testing our procedure with a simplistic synthetic signal; we do not attempt to model the merger and ringdown stages, which occur in a very short time, when compared with the working window in the inspiral phase.

The signal is injected by choosing the angles in the celestial sphere to agree with a different delay ring, and for simplicity we have chosen arbitrarily the orientation of the GW to be given by the frame determined by $\Delta\psi = 0$.

For the general case $e \neq 0$ we follow Peters (1964) and express

$$a(e) = a_0 \left(\frac{e}{e_0}\right)^{12/19} \left(\frac{1 - e_0^2}{1 - e^2}\right) \left(\frac{1 + \frac{121}{304}e^2}{1 + \frac{121}{304}e_0^2}\right)^{870/2299}, \quad (80)$$

and

$$\frac{de}{dt} = -\frac{19}{12} \frac{\beta}{c_0^4} \frac{e^{-29/19} (1 - e^2)^{3/2}}{\left(1 + \frac{121}{304}e^2\right)^{1181/2299}}, \quad (81)$$

with

$$c_0 = a_0 \left(\frac{1 - e_0^2}{e_0^{12/19} \left(1 + \frac{121}{304}e_0^2\right)^{870/2299}}\right), \quad (82)$$

and

$$\beta = \frac{64G^3 m_1 m_2 (m_1 + m_2)}{5c^5}; \quad (83)$$

where a_0 and e_0 are the corresponding initial values.

One also needs to integrate

$$\frac{d\phi}{dt} = \sqrt{GM} \frac{(1 + e \cos(\phi - \phi_0))^2}{\sqrt{a^3 (1 - e^2)^3}}, \quad (84)$$

and for completeness we also mention that the radial coordinate is

$$r = \frac{a(1 - e^2)}{1 + e \cos(\phi - \phi_0)}, \quad (85)$$

the orbital period is

$$P = 2\pi \sqrt{\frac{a^3}{GM}}; \quad (86)$$

and the instantaneous orbital frequency can be written as

$$\nu \equiv \dot{\phi} = \frac{2\pi}{P} \frac{(1 + e \cos(\phi - \phi_0))^2}{\sqrt{(1 - e^2)^3}}. \quad (87)$$

As a validation of our procedure, for the location of a GW source with spin-2 polarization, we have applied it to this peculiar case of synthetic signal with $a_0 = 12(m_1 + m_2)$ and $e_0 = 0.35$, where the resulting synthetic polarization modes are shown in Fig. 60.

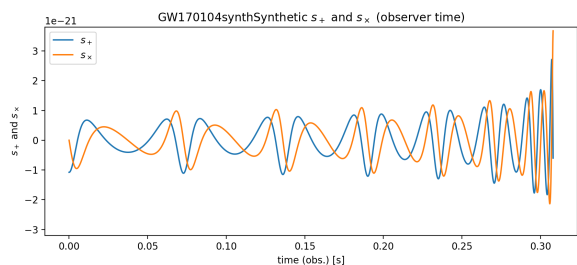


Fig. 60 Injected + and \times polarization modes.

Also, as a validation of our procedure, for the fidelity in the measurement of the PM, the results in reconstructing the gravitational-wave polarization modes of this synthetic signal are shown in the main text in Figs. 31 and 32; where one can check an excellent agreement.

References

- Abbott BP, et al (2016a) GW150914: First results from the search for binary black hole coalescence with Advanced LIGO. Phys Rev D 93(12):122003. <https://doi.org/10.1103/PhysRevD.93.122003>, arXiv:1602.03839 [gr-qc]
- Abbott BP, et al (2016b) Observation of Gravitational Waves from a Binary Black Hole Merger. Phys Rev Lett 116(6):061102. <https://doi.org/10.1103/PhysRevLett.116.061102>, arXiv:1602.03837 [gr-qc]
- Abbott BP, et al (2016c) Tests of general relativity with GW150914. Phys Rev Lett 116(22):221101. <https://doi.org/10.1103/PhysRevLett.116.221101>, [Erratum: Phys.Rev.Lett. 121, 129902 (2018)], arXiv:1602.03841 [gr-qc]
- Abbott BP, et al (2017a) Calibration of the Advanced LIGO detectors for the discovery of the binary black-hole merger GW150914. Phys Rev D 95(6):062003. <https://doi.org/10.1103/PhysRevD.95.062003>, arXiv:1602.03845 [gr-qc]
- Abbott BP, et al (2017b) GW170104: Observation of a 50-Solar-Mass Binary Black Hole Coalescence at Redshift 0.2. Phys Rev Lett 118(22):221101. <https://doi.org/10.1103/PhysRevLett.118.221101>, arXiv:1706.01812 [gr-qc]

- Abbott BP, et al (2017c) GW170814: A Three-Detector Observation of Gravitational Waves from a Binary Black Hole Coalescence. *Phys Rev Lett* 119(14):141101. <https://doi.org/10.1103/PhysRevLett.119.141101>, [arXiv:1709.09660](https://arxiv.org/abs/1709.09660) [gr-qc]
- Abbott BP, et al (2018) Search for Tensor, Vector, and Scalar Polarizations in the Stochastic Gravitational-Wave Background. *Phys Rev Lett* 120(20):201102. <https://doi.org/10.1103/PhysRevLett.120.201102>, [arXiv:1802.10194](https://arxiv.org/abs/1802.10194) [gr-qc]
- Abbott BP, et al (2020) Prospects for observing and localizing gravitational-wave transients with Advanced LIGO, Advanced Virgo and KAGRA. *Living Rev Rel* 23(3):69. <https://doi.org/10.1007/s41114-020-00026-9>
- Abbott R, et al (2021) Open data from the first and second observing runs of Advanced LIGO and Advanced Virgo. *SoftwareX* 13:100658. <https://doi.org/10.1016/j.softx.2021.100658>, [arXiv:1912.11716](https://arxiv.org/abs/1912.11716) [gr-qc]
- Abbott R, et al (2023) Open Data from the Third Observing Run of LIGO, Virgo, KAGRA, and GEO. *Astrophys J Suppl* 267(2):29. <https://doi.org/10.3847/1538-4365/acdc9f>, [arXiv:2302.03676](https://arxiv.org/abs/2302.03676) [gr-qc]
- Albert A, et al (2017) All-sky search for high-energy neutrinos from gravitational wave event GW170104 with the Antares neutrino telescope. *Eur Phys J C* 77(12):911. <https://doi.org/10.1140/epjc/s10052-017-5451-z>, [arXiv:1710.03020](https://arxiv.org/abs/1710.03020) [astro-ph.HE]
- Allen B, Anderson WG, Brady PR, et al (2012) FINDCHIRP: An Algorithm for detection of gravitational waves from inspiraling compact binaries. *Phys Rev D* 85:122006. <https://doi.org/10.1103/PhysRevD.85.122006>, [arXiv:gr-qc/0509116](https://arxiv.org/abs/gr-qc/0509116) [gr-qc]
- Ashby N (2003) Relativity in the Global Positioning System. *Living Rev Rel* 6:1. <https://doi.org/10.12942/lrr-2003-1>
- Bacon P, Trovato A, Bejger M (2023) Denoising gravitational-wave signals from binary black holes with a dilated convolutional autoencoder. *Mach Learn Sci Tech* 4(3):035024. <https://doi.org/10.1088/2632-2153/acd90f>, [arXiv:2205.13513](https://arxiv.org/abs/2205.13513) [gr-qc]
- Bartos I, Bork R, Factourovich M, et al (2010) The Advanced LIGO timing system. *Class Quant Grav* 27:084025. <https://doi.org/10.1088/0264-9381/27/8/084025>
- Bradt H (2004) *Astronomy Methods: A Physical Approach to Astronomical Observations*. Cambridge Planetary Science, Cambridge University Press
- Casella G, Berger RL (2002) *Statistical Inference*, 2nd edn. DUXBURY
- Chatterjee C, Jani K (2024) Reconstruction of Binary Black Hole Harmonics in LIGO Using Deep Learning. *Astrophys J* 969(1):25. <https://doi.org/10.3847/1538-4357/ad4602>, [arXiv:2403.01559](https://arxiv.org/abs/2403.01559) [gr-qc]
- Chatterjee C, Kovalam M, Wen L, et al (2023) Rapid Localization of Gravitational Wave Sources from Compact Binary Coalescences Using Deep Learning. *Astrophys J* 959(1):42. <https://doi.org/10.3847/1538-4357/ad08b7>, [arXiv:2207.14522](https://arxiv.org/abs/2207.14522) [gr-qc]
- Chatterji S, Lazzarini A, Stein L, et al (2006) Coherent network analysis technique for discriminating gravitational-wave bursts from instrumental noise. *Phys Rev D* 74:082005. <https://doi.org/10.1103/PhysRevD.74.082005>, [arXiv:gr-qc/0605002](https://arxiv.org/abs/gr-qc/0605002)
- Cohen A, Daubechies I, Feauveau JC (1992) Biorthogonal bases of compactly supported wavelets. *Communications on pure and applied mathematics* 45(5):485–560
- Cornish NJ, Littenberg TB (2015) BayesWave: Bayesian Inference for Gravitational Wave Bursts and Instrument Glitches. *Class Quant Grav* 32(13):135012. <https://doi.org/10.1088/0264-9381/32/13/135012>, [arXiv:1410.3835](https://arxiv.org/abs/1410.3835) [gr-qc]
- Cutler C, Flanagan EE (1994) Gravitational waves from merging compact binaries: How accurately can one extract the binary’s parameters from the inspiral wave form? *Phys Rev D* 49:2658–2697. <https://doi.org/10.1103/PhysRevD.49.2658>, [arXiv:gr-qc/9402014](https://arxiv.org/abs/gr-qc/9402014) [gr-qc]
- Donoho DL, Johnstone IM (1994) Ideal spatial adpatation by wavelet shrinkage. *Biometrika* 81(3)(3):425–455. <https://doi.org/10.1093/biomet/81.3.425>
- Eardley DM, Lee DL, Lightman AP (1973a) Gravitational-wave observations as a tool for testing relativistic gravity. *Phys Rev D* 8:3308–3321. <https://doi.org/10.1103/PhysRevD.8.3308>
- Eardley DM, Lee DL, Lightman AP, et al (1973b) Gravitational-wave observations as a tool for testing relativistic gravity. *Phys Rev Lett* 30:884–886. <https://doi.org/10.1103/PhysRevLett.30.884>
- Einstein A (1911) Über den Einfluß der Schwerkraft auf die Ausbreitung des Lichtes. *Annalen der Physik* 340(10):898–908
- Fairhurst S (2009) Triangulation of gravitational wave sources with a network of detectors. *New J of Physics* 11:123006. <https://doi.org/10.1088/1367-2630/11/12/123006>, [arXiv:0908.2356](https://arxiv.org/abs/0908.2356) [gr-qc]

- Fairhurst S (2011) Source localization with an advanced gravitational wave detector network. *Class Quant Grav* 28:105021. <https://doi.org/10.1088/0264-9381/28/10/105021>, [arXiv:1010.6192](https://arxiv.org/abs/1010.6192) [gr-qc]
- Ferguson TS (1967) *Mathematical Statistics: A Decision Theoretic Approach*. Academic Press
- Geroch R, Held A, Penrose R (1973) A space-time calculus based on pairs of null directions. *J Math Phys* 14:874–881
- Goldstein A, et al (2017) Fermi Observations of the LIGO Event GW170104. *Astrophys J Lett* 846(1):L5. <https://doi.org/10.3847/2041-8213/aa8319>, [arXiv:1706.00199](https://arxiv.org/abs/1706.00199) [astro-ph.HE]
- Gürsel Y, Tinto M (1989) Near optimal solution to the inverse problem for gravitational-wave bursts. *PhysRevD* 40(12):3884–3938
- Helstrom CW (1975) *Statistical theory of signal detection*, 2nd edn. Pergamon Press
- Hu Q, Zhou C, Peng JH, et al (2021) Semianalytical approach for sky localization of gravitational waves. *Phys Rev D* 104(10):104008. <https://doi.org/10.1103/PhysRevD.104.104008>, [arXiv:2110.01874](https://arxiv.org/abs/2110.01874) [gr-qc]
- Jaranowski P, Krolak A (2009) *Analysis of gravitational-wave data*. Cambridge Univ. Press, Cambridge, <https://doi.org/10.1017/CBO9780511605482>
- Klimenko S, Vedovato G, Drago M, et al (2011) Localization of gravitational wave sources with networks of advanced detectors. *Phys Rev D* 83:102001. <https://doi.org/10.1103/PhysRevD.83.102001>, [arXiv:1101.5408](https://arxiv.org/abs/1101.5408) [astro-ph.IM]
- Klimenko S, et al (2016) Method for detection and reconstruction of gravitational wave transients with networks of advanced detectors. *Phys Rev D* 93(4):042004. <https://doi.org/10.1103/PhysRevD.93.042004>, [arXiv:1511.05999](https://arxiv.org/abs/1511.05999) [gr-qc]
- Kolmus A, Baltus G, Janquart J, et al (2022) Fast sky localization of gravitational waves using deep learning seeded importance sampling. *Phys Rev D* 106(2):023032. <https://doi.org/10.1103/PhysRevD.106.023032>, [arXiv:2111.00833](https://arxiv.org/abs/2111.00833) [gr-qc]
- Lee GR, Gommers R, Waselewski F, et al (2019) PyWavelets: A Python package for wavelet analysis. *Journal of Open Source Software* 4(36)(1237):1–2. <https://doi.org/10.21105/joss.01237>
- LIGO (2017) LIGO Document T1700179-v1, GW170104 sky localization. <https://dcc.ligo.org/LIGO-T1700179/public>, [Online; accessed 28-May-2024]
- Mallat S (2009) *A Wavelet Tour of Signal Processing: The Sparse Way*. Elsevier Inc.
- McDonough RN, Whalen AD (1995) *Detection of Signals in Noise*, 2nd edn. Academic Press
- Moreschi OM (1987) General future asymptotically flat spacetimes. *Class Quantum Grav* 4:1063–1084
- Moreschi OM (2004) Intrinsic angular momentum and center of mass in general relativity. *ClassQuantum Grav* 21:5409–5425. <https://doi.org/10.1088/0264-9381/21/23/008>
- Moreschi OM (2019) Convenient filtering techniques for LIGO strain of the GW150914 event. *JCAP* 1904:032. <https://doi.org/10.1088/1475-7516/2019/04/032>, [arXiv:1903.00546](https://arxiv.org/abs/1903.00546) [gr-qc]
- Moreschi OM (2024) Comparison of unknown gravitational-wave signals in two detectors. *Astrophys Space Sci* 369(1):12. <https://doi.org/10.1007/s10509-024-04276-9>
- Moreschi OM (2025) Localization of GW190521 and reconstruction of the spin-2 gravitational-wave polarization modes [arXiv:2504.00207](https://arxiv.org/abs/2504.00207) [gr-qc]
- Nishizawa A, Taruya A, Hayama K, et al (2009) Probing non-tensorial polarizations of stochastic gravitational-wave backgrounds with ground-based laser interferometers. *Phys Rev D* 79:082002. <https://doi.org/10.1103/PhysRevD.79.082002>, [arXiv:0903.0528](https://arxiv.org/abs/0903.0528) [astro-ph.CO]
- Penrose R, Rindler W (1984) *Spinors and Space-Time*, vol 1. Cambridge University Press, Cambridge
- Peters PC (1964) Gravitational Radiation and the Motion of Two Point Masses. *Phys Rev* 136:B1224–B1232. <https://doi.org/10.1103/PhysRev.136.B1224>
- Petit G, Luzum B, (Eds.) (2010) *International Earth Rotation and Reference Systems Service (IERS)*. URL <https://iers-conventions.obspm.fr/content/tn36.pdf>, technical Note No. 36
- Pirani FAE (1965) Introduction to gravitational radiation theory. In: Trautman A, Pirani FAE, Bondi H (eds) *Brandeis Summer Institute in Theoretical Physics 1964, Volume One: Lectures on general relativity*. Prentice-Hall Inc., p 249–373
- Poisson E, Will CM (2014) *Gravity: Newtonian, Post-Newtonian, Relativistic*. Cambridge University Press
- Savchenko V, et al (2017) INTEGRAL observations of GW170104. *Astrophys J Lett* 846(2):L23. <https://doi.org/10.3847/2041-8213/aa87ae>, [arXiv:1707.03719](https://arxiv.org/abs/1707.03719) [astro-ph.HE]

- Singer LP, Price LR (2016) Rapid Bayesian position reconstruction for gravitational-wave transients. *Phys Rev D* 93(2):024013. <https://doi.org/10.1103/PhysRevD.93.024013>, [arXiv:1508.03634](https://arxiv.org/abs/1508.03634) [gr-qc]
- Stalder B, et al (2017) Observations of the GRB afterglow ATLAS17aeu and its possible association with GW170104. *Astrophys J* 850(2):149. <https://doi.org/10.3847/1538-4357/aa95c1>, [arXiv:1706.00175](https://arxiv.org/abs/1706.00175) [astro-ph.HE]
- Takeda H, Nishizawa A, Michimura Y, et al (2018) Polarization test of gravitational waves from compact binary coalescences. *Phys Rev D* 98(2):022008. <https://doi.org/10.1103/PhysRevD.98.022008>, [arXiv:1806.02182](https://arxiv.org/abs/1806.02182) [gr-qc]
- Touboul P, et al (2022) Result of the MICROSCOPE weak equivalence principle test. *Class Quant Grav* 39(20):204009. <https://doi.org/10.1088/1361-6382/ac84be>, [arXiv:2209.15488](https://arxiv.org/abs/2209.15488) [gr-qc]
- Tsutsui T, Cannon K, Tsukada L (2021) High speed source localization in searches for gravitational waves from compact object collisions. *Phys Rev D* 103(4):043011. <https://doi.org/10.1103/PhysRevD.103.043011>, [arXiv:2005.08163](https://arxiv.org/abs/2005.08163) [astro-ph.HE]
- Veitch J, et al (2015) Parameter estimation for compact binaries with ground-based gravitational-wave observations using the LALInference software library. *Phys Rev D* 91(4):042003. <https://doi.org/10.1103/PhysRevD.91.042003>, [arXiv:1409.7215](https://arxiv.org/abs/1409.7215) [gr-qc]
- Verrecchia F, et al (2017) AGILE Observations of the Gravitational Wave Source GW170104. *Astrophys J Lett* 847(2):L20. <https://doi.org/10.3847/2041-8213/aa8224>, [arXiv:1706.00029](https://arxiv.org/abs/1706.00029) [astro-ph.HE]
- Wald R (1984) *General Relativity*. The Chicago University Press
- Wen L, Chen Y (2010) Geometrical Expression for the Angular Resolution of a Network of Gravitational-Wave Detectors. *Phys Rev D* 81:082001. <https://doi.org/10.1103/PhysRevD.81.082001>, [arXiv:1003.2504](https://arxiv.org/abs/1003.2504) [astro-ph.CO]
- You ZQ, Ashton G, Zhu XJ, et al (2021) Optimized localization for gravitational waves from merging binaries. *Mon Not Roy Astron Soc* 509(3):3957–3965. <https://doi.org/10.1093/mnras/stab2977>, [arXiv:2105.04263](https://arxiv.org/abs/2105.04263) [gr-qc]